PI3Kβ controls immune evasion in PTEN-deficient breast tumors

Johann S. Bergholz[1,2,3,*], **Qiwei Wang**[1,2,3,*], **Qi Wang**[1,*], **Michelle Ramseier**[3,4,5], **Sanjay Prakadan**[3,4,5], **Weihua Wang**[1], **Rong Fang**[1,6], **Sheheryar Kabraji**[1,7,8], **Qian Zhou**[9], **G. Kenneth Gray**[10], **Kayley Abell-Hart**[1], **Shaozhen Xie**[1,2], **Xiaocan Guo**[1,2], **Hao Gu**[1,2], **Thanh Von**[1], **Tao Jiang**[1], **Shuang Tang**[1,2,9], **Gordon J. Freeman**[7], **Hye-Jung Kim**[11,12], **Alex K. Shalek**[3,4,5], **Thomas M. Roberts**[1,2,§], **Jean J. Zhao**[1,2,3,§]

[1]Department of Cancer Biology, Dana-Farber Cancer Institute, Boston, MA, USA

2Department of Biological Chemistry and Molecular Pharmacology, Harvard Medical School, Boston, MA, USA

3Broad Institute of Harvard and MIT, Cambridge, MA, USA

4Institute for Medical Engineering and Science (IMES), Department of Chemistry, and Koch Institute for Integrative Cancer Research, MIT, Cambridge, MA, USA

5Ragon Institute of MGH, MIT, and Harvard, Cambridge, MA, USA

6Ningbo Clinical Pathology Diagnosis Center, Ningbo, Zhejiang 315211, P.R. China

7Department of Medical Oncology, Dana-Farber Cancer Institute, Boston, MA, USA

8Laboratory of Systems Pharmacology, Harvard Medical School, Boston, MA, USA

9Cancer Institute, Fudan University Shanghai Cancer Center, Shanghai 200032, P.R. China

10Department of Cell Biology and Ludwig Center at Harvard, Harvard Medical School, Boston, MA, USA

11Department of Cancer Immunology and Virology, Dana-Farber Cancer Institute, Boston, MA, USA

12Department of Immunology Discovery, Genentech, South San Francisco, CA, USA

Abstract

Loss of the PTEN tumor suppressor is one of the most common oncogenic drivers across all cancer types[1]. PTEN is the major negative regulator of phosphoinositide-3 kinase (PI3K) signaling. Notably, the PI3Kβ isoform has been shown to play an important role in PTEN-deficient tumors, but the mechanisms underlying the importance of PI3Kβ activity remain elusive. Using a syngeneic genetically-engineered mouse (GEM) model of invasive breast cancer driven by concurrent ablation of *Pten* and *Trp53* (p53), we showed that genetic inactivation of PI3Kβ led to a robust anti-tumor immune response that abrogated tumor growth in syngeneic immunocompetent mice, but not in immunodeficient mice. Mechanistically, PI3Kβ inactivation in the PTEN-null setting led to reduced STAT3 signaling and increased expression of immune stimulatory molecules, thereby promoting anti-tumor immune responses. Pharmacological PI3Kβ inhibition also elicited anti-tumor immunity, and synergized with immunotherapy to inhibit tumor growth. Mice with complete responses to the combined treatment displayed immune memory and rejected tumors upon re-challenge. Our findings demonstrate a molecular mechanism linking PTEN loss and STAT3 activation in cancer and suggest that PI3Kβ controls immune escape in PTEN-null tumors, providing a rationale for combining PI3Kβ inhibitors with immunotherapy for the treatment of PTEN-deficient breast cancer.

PTEN deficiency plays an important role in mediating immune evasion[2,3]. Loss of PTEN has been reported to promote immune suppression and therapeutic resistance to immunotherapy in various cancer types[4–6]. Previous studies using genetic approaches and pharmacological inhibition demonstrated that PTEN-null tumors often depend on the p110β catalytic isoform of PI3K (PI3Kβ) for tumor formation[7–9]. However, the roles of the two major catalytic isoforms of PI3K, namely p110α (PI3Kα) and PI3Kβ, in immune evasion

induced by PTEN loss remain unknown. Here, we report that PI3Kβ is a prime mediator of immune evasion in PTEN-null breast cancer, and that PI3Kβ inhibition sensitizes tumor cells to immunotherapy.

PI3Kβ is required for immune evasion

To better understand how specific isoforms of PI3K affect immune responses to PTEN-deficient tumors, we developed a syngeneic GEM model of breast cancer driven by concurrent loss of PTEN and p53 (*Trp53*) in mammary epithelial cells through Keratin 14 (K14)-mediated Cre recombination to delete homozygous floxed *Pten* and *Trp53* alleles (designated PP; Fig. 1a). To circumvent deleterious effects on the epidermis due to loss of PTEN in keratinocytes[10], we transplanted mammary tissue from PP mice into the cleared mammary fat pads of athymic nude mice (immunocompromised mice lacking T-cells) to facilitate tumor growth (Fig. 1b). Histological analyses revealed that PP tumors were highly cellular anaplastic invasive adenocarcinomas (Extended Data Fig.1a). Notably, genetic inactivation of *PTEN* and *TP53* (p53) are two of the most frequent alterations found in invasive basal breast cancer[11,], and the vast majority of cases with PTEN loss show concomitant p53 inactivation (Extended Data Fig. 1b). Thus, our PP model recapitulates both the genetics and pathology of an important percentage of breast cancers of the basal subtype seen in the clinic.

We generated two more tumor models with additional deletion of *Pik3ca* (p110α) or *Pik3cb* (p110β; denoted PPA and PPB, respectively; Fig. 1a–b). PPA tumors showed spindle cell morphology with elongated cytoplasm extending to each side of small and slightly pleiomorphic nuclei, indicative of mesenchymal morphology and resembling sarcoma-like histology, while PPB tumors resembled adenocarcinomas with large pleiomorphic nuclei and little cytoplasm (Extended Data Fig.1a). We then derived primary tumor cell cultures for subsequent mechanistic and transplantation experiments. Characterization of these primary tumor cells confirmed PTEN, p53 and PI3K isoform ablation, as well as selective PI3K isoform signaling for each model (Extended Data Fig. 1c–e). PP tumor cells express intermediate levels of the epithelial marker E-cadherin and the mesenchymal marker vimentin, while PPA cells express high levels of vimentin and undetectable E-cadherin, and PPB cells express high E-cadherin and very low vimentin (Extended Data Fig. 1f), suggesting significant divergence in epithelial/mesenchymal phenotypes that could contribute to differences in disease progression.

We transplanted PP, PPA or PPB tumor cells orthotopically into syngeneic immunocompetent mice (FVB strain) and into nude mice. We found that PP tumors grew faster in the immunocompromised mice relative to the immunocompetent mice (Fig. 1c), suggesting these tumors could be subject to initial attack by the immune system, but that resistance quickly develops. PPA tumors did not exhibit differences in growth rate between nude and FVB mice (Fig. 1d). Surprisingly, PPB tumors completely failed to grow in immunocompetent mice, but formed tumors in nude mice (Fig. 1e and Extended Data Fig. 1g), suggesting that PI3Kβ is critical for mediating immune evasion in a PTEN-null setting. We confirmed these results by transplanting PPB tumor cells into syngeneic FVB mice lacking adaptive immunity due to genetic *Rag1* deletion, in which case tumors formed in

mice with homozygous but not heterozygous *Rag1* deletion (Extended Data Fig. 1h). We confirmed that rejection of PPB tumors by immunocompetent mice is due to genetic deletion of the PI3Kβ gene by reintroducing mouse PI3Kβ into PPB tumor cells (PPB-mPI3Kβ; Extended data Fig. 1i). While PPB cells expressing a vector control failed to form tumors in FVB mice, transplanting PPB-mPI3Kβ cells resulted in tumor growth with a similar growth rate to PP tumors in FVB mice, albeit with 80% penetrance (Fig. 1c and Extended data Fig. 1j–k). To further investigate the role of T-cells in tumor rejection, we injected FVB mice with PPB tumor cells and treated with either CD4 or CD8 depleting antibodies. Although anti-CD4 treatment induced a slight delay in tumor rejection, all PPB tumors were eventually rejected, while anti-CD8 treatment prevented tumor rejection and resulted in 100% tumor penetrance (Extended data Fig. 1l), suggesting that that CD8+ T-cells are required to reject PPB tumors.

We found that PPB tumors grow more slowly than PP and PPA tumors in nude mice. Consistently, PPB tumor cells proliferated at a slower rate *in vitro* (Extended Data Fig. 2a). Tissue-based cyclic immunofluorescence (CyCIF) analysis of GFP-tagged PP, PPA and PPB tumors five days after transplantation into nude mice (to avoid T-cell-mediated cytotoxicity) revealed distinctly reduced levels of proliferation markers in PPB tumor cells and no significant differences in cleaved caspase 3; moreover, the percentage of Ki67/MCM2 double-positive PP and PPA tumor cells ranged from approximately 25% to 45%, compared to ~10% for PPB tumor cells (Extended Data Fig. 2b–c). These observations suggest that differences in proliferation potential are likely to account for differences in tumor growth rate between models. Interestingly, a significantly higher percentage of PPB tumor cells stained positive for γH2AX (1.5–2%) compared to ~0.6% in PP and ~0.3% in PPA tumors (Extended Data Fig. 2b–c). Increased DNA damage in PPB cells could also contribute to reduced growth of PPB tumors.

PI3Kβ mediates immune suppression

To investigate the differential immune responses to PP, PPA and PPB tumors, we analyzed tumors five days after transplantation into FVB mice. CyCIF revealed that, while PP and PPA cells formed tumors with strong phospho-AKT (P-AKT) signals in which CD4+ and CD8+ T-cells were largely excluded to the periphery, PPB tumors displayed only a few residual tumor cells with markedly high levels of CD4+ and CD8+ T-cells infiltrating the tumor bed (Fig. 2a).

We then took an unbiased approach to analyze the immune infiltrate by single-cell RNA-sequencing (scRNA-Seq). Strikingly, the composition of immune cells differed vastly among models (Fig. 2b and Extended Data Fig. 3a–c). Clustering of T-cells identified a PPB-enriched cluster (T_1) that was virtually undetectable in the other two models and was defined by differential expression of interferon (IFN) response genes associated with T-cell activation[12,13] (Fig. 2c). Other T-cell clusters corresponding to regulatory T-cells (Tregs; T_2), bystander CD4+ T-cells (T_3), and activated γδ T-cells (T_4) were found in both PP and PPB tumors, while the small number of PPA-associated T-cells were largely in cluster T_3 (Fig. 2c). Gene set enrichment analysis (GSEA) corroborated these phenotypes (Fig. 2d).

We also examined dendritic cells (DCs) in more detail, as these are the major antigen-presenting cell population fundamental for T-cell priming and activation[14]. Plasmacytoid dendritic cells (pDCs), a specialized cell population known to secrete large quantities of type I IFNs in response to viral infection[14], were primarily found in PPB tumors (Fig. 2b and Extended Data Fig. 3c). While the numbers of classical DCs (cDCs) from PP, PPA and PPB tumors were similar (Fig. 2b and Extended Data Fig. 3c), differential gene expression (DGE) analysis revealed that PPB-associated cDCs differentially expressed genes related to antigen presentation via major histocompatibility complex (MHC) class I and MHC class II (MHC-I/II) compared to cDCs from PP and PPA tumors (Fig. 2e). Consistently, the top canonical pathway up-regulated in cDCs from PPB tumors was antigen presentation, followed by pathways related to DC maturation and IFN signaling (Fig. 2f).

Monocytes and macrophages (MoMϕ) had phenotypes consistent with the ones determined for T-cells and cDCs in each tumor type. The majority of MoMϕ from PPB tumors were characterized by high expression of IFN-responsive genes, MHC-I/II genes and markers of inflammatory monocytes (cluster MoMϕ_1), while MoMϕ from PP and PPA tumors primarily showed characteristics resembling anti-inflammatory tumor-associated macrophage (TAM) differentiation, including subsets with increased expression of genes implicated in immune suppression (MoMϕ_2) or proliferation (MoMϕ_4) found predominantly in PPA tumors, and a PP-enriched cluster associated with oxidative phosphorylation and complement immune response (MoMϕ_5; Extended Data Fig. 4a–e)[15–17].

Flow cytometry confirmed that T-cell activation was stronger in PPB and weaker in PPA tumors, as shown by increased levels of effector T-cells, IFNγ production and proliferation (Extended Data Fig. 5a). PPB tumors were also more highly infiltrated by Tregs (Extended Data Fig. 5a), which is consistent with our scRNA-Seq data and previous findings showing that Tregs accumulate at sites of strong CD8+ T-cell activation to regulate immune activation[18]. Although total DC levels were similar among models, PPB tumors demonstrated enhanced DC activation and maturation, as evidenced by increased IRF3 phosphorylation (P-IRF3), and elevated MHC-II and CD80/CD86 co-stimulatory ligands (Extended Data Fig. 5b). Guided by our scRNA-Seq, we confirmed that myeloid cells in PPB tumors produced significantly higher levels of IFNγ, that PPB tumors are significantly more infiltrated by inflammatory monocytes, and that these inflammatory monocytes account for the vast majority of IFNγ produced by myeloid cells and express higher levels of MHC-I (Extended Data Fig. 5c–g). To determine potential differences in response to IFNγ, we treated tumor cells with IFNγ *in vitro*. As expected, IFNγ induced up-regulation of MHC-I and dose-dependent decreases in tumor cell viability; however, we did not detect differences in response to IFNγ between PP, PPA and PPB tumor cells (Extended Data Fig. 5h–i). These data indicate that PPB tumors have strong IFN signaling in both the myeloid and lymphoid compartments, resulting in an IFN-mediated anti-tumor immune response.

PPB tumor cells activate DCs *ex vivo*

We sought to assess how tumor cells interact with immune cells *ex vivo*. We co-cultured PP or PPB tumor cells with bone marrow-derived cells (BMCs) harvested from naïve

mice. Strikingly, these BMCs exhibited a marked increase in the proportion of DC differentiation (CD11c+ MHC-II[High]) and activation (CD80[High] CD86[High]) when they were co-cultured with PPB, but not PP, tumor cells, despite the absence of exogenous agents that could stimulate DC development, such as FMS-like tyrosine kinase 3 ligand (FLT-3L) or granulocyte-macrophage colony-stimulating factor (GM-CSF; Extended Data Fig. 6a)[19]. Moreover, PPB tumor cells markedly up-regulated DC activation markers when they were co-cultured with bone marrow-derived dendritic cells (BMDCs) from naïve mice, compared to PP cells (Extended Data Fig. 6b). We then co-cultured naïve splenic CD8+ T-cells with PP or PPB tumor cells and did not detect differences in CD8+ T-cell activation (Extended Data Fig. 6c). However, sequential co-culturing of BMDCs with tumor cells and then with CD8+ T-cells showed that BMDCs co-cultured with PPB cells promoted significantly more CD8+ T-cell activation than BMDCs co-cultured with PP tumor cells (Extended Data Fig. 6d). Taken together, these results support the hypothesis that ablating PI3Kβ in PTEN-deficient breast tumor cells promotes both the differentiation of myeloid cells into DCs and the activation of intra-tumoral DCs, which can effectively activate T-cells.

PI3Kβ suppresses immunity via STAT3

We next profiled gene expression of PP and PPB cells cultured *in vitro* to explore mechanisms by which PI3Kβ inactivation affects immune evasion. Bulk RNA-seq showed that numerous genes involved in immune responses, including cytokines, regulators of TNFα and Toll-like receptor (TLR) signaling, antigen processing, and immune stimulation were significantly up-regulated in PPB compared to PP cells, while multiple immune suppressive genes were down-regulated (Extended Data Fig. 6e). The expression and secretion of GM-CSF (*Csf2*) were markedly higher in PPB cells (Extended Data Fig. 6e–f). Since GM-CSF is critical for DC development and activation[20], this suggests a potential mechanism by which PPB tumors could activate DCs. Consistently, GM-CSF signaling was up-regulated in cDCs from PPB tumors *in vivo* (Fig. 2f). Ingenuity pathway analysis (IPA) likewise showed up-regulated GM-CSF signaling in PPB tumor cells, in addition to other immune-related pathways, while down-regulated signaling included pathways associated with immune suppression[21] (Fig. 3a). Notably, STAT3 signaling was the top down-regulated canonical pathway in PPB compared to PP cells. GSEA similarly revealed down-regulated IL6-JAK-STAT3 and up-regulated TNFα signaling via NF-κB signatures in PPB cells compared to PP (Fig. 3b). We found similar results by transcriptome analysis of PP and PPB tumor cells isolated from tumor-bearing nude mice, including up-regulation of signatures involved in IFN and inflammatory signaling and down-regulation of pathways associated with immune suppression in PPB tumor cells (Fig. 3c–d). Consistently, IL-6 expression and STAT3 activation (as assessed by Tyr[705] phosphorylation) were significantly lower in PPB tumor cells *in vitro* and *in vivo* (Fig. 3e–g and Extended Data Fig. 6g–i).

To investigate the involvement of STAT3 activation in PI3Kβ-mediated signaling, we expressed a constitutively active STAT3[A661C, N663C] (STAT3-CA) construct in PPB cells (Extended Data Fig. 7a). STAT3-CA expression down-regulated many immunostimulatory genes, including cytokines and mediators of TNFα signaling and immune stimulation (Extended Data Fig. 7b). GSEA also revealed down-regulated signatures of inflammatory response and TNFα signaling via NF-κB in PPB-STAT3-CA cells (Extended Data Fig. 7c).

Moreover, PPB-STAT3-CA cells showed decreased production of GM-CSF and reduced ability to activate DCs in co-culture (Extended Data Fig. 7d–e). Conversely, silencing *Stat3* expression in PP cells via shRNA up-regulated expression of immunostimulatory genes and signatures of inflammatory response and TNFα signaling via NF-κB, and led to increased GM-CSF secretion and activation of co-cultured DCs (Extended Data Fig. 7f–j). Similar to genetic deletion of PI3Kβ, silencing Stat3 expression slowed PP tumor growth in nude mice (Extended Data Fig. 7k). In FVB mice, PP-shStat3 tumors exhibited a marked delay in reaching exponential tumor growth (~8 weeks) compared to control PP-shGFP tumors (~2 weeks), with complete rejection of 16–37% of PP-shStat3 tumors (3/8 for shStat3–1, and 1/6 for shStat3–2; Extended Data Fig. 7k). Moreover, PP-shStat3 tumors exhibited higher levels of T-cell infiltration and activation than PP-shGFP tumors, as evidenced by enhanced IFNγ production and proliferation (Extended Data Fig. 7l).

To assess whether pharmacologic inhibition of PI3Kβ can recapitulate the findings observed through genetic inactivation, we treated PP cells with the PI3Kβ-selective inhibitor AZD6482 (also known as KIN193[8]). These and subsequent *in vitro* experiments were conducted under serum/nutrient starvation conditions to avoid extraneous variables affecting signaling downstream of PI3K that prevent effective evaluation of pharmacological PI3Kβ inhibition (Extended Data Fig. 8a). AZD6482 treatment reduced P-AKT and P-STAT3^{Y705} as well as STAT3 nuclear translocation in PP cells (Fig. 3h). AZD6482 treatment also resulted in up-regulation of genes involved in immune response and down-regulation of immune suppressive genes (Extended Data Fig. 8b), as well as enriched GSEA signatures of inflammatory response and TNFα signaling via NF-κB (Fig. 3i), and up-regulated GM-CSF and down-regulated IL-6 (Extended Data Fig. 8c). Similarly, *in vivo* treatment with AZD6482 up-regulated of TNFα/NF-κB signaling and down-regulated IL-6/STAT3 signaling signatures in PP tumor cells isolated from tumor-bearing nude mice (Extended Data Fig. 8d). PI3Kβ inhibition also down-regulated AKT and STAT3 phosphorylation in PTEN-deficient human breast cancer cell lines *in vitro* and *in vivo* (Extended Data Fig. 8e–f). Taken together, these results indicate that PI3Kβ regulates a program of immune resistance in PTEN-deficient breast tumor cells that is chiefly mediated by STAT3.

To investigate the molecular mechanisms by which PI3Kβ induces STAT3 activation, we first treated PP cells with the AKT-specific inhibitor MK2206, which strongly inhibited AKT phosphorylation, but did not affect STAT3^{Y705} phosphorylation (Extended Data Fig. 8g), suggesting that AKT down-regulation is not required to reduce STAT3 activation by PI3Kβ inhibition. Further examination of our IPA results revealed down-regulation of TEC Kinase signaling in PPB cells compared to PP cells (Fig. 3a). TEC Kinases contain a PH domain and can be activated downstream of PI3K[22]. Notably, the TEC Kinase family member BMX (also known as ETK) has been shown to activate STAT3[23], and pharmacological treatment with either the TEC Kinase inhibitor LFM-A13 or the pan-PI3K inhibitor GDC-0914 was reported to decrease STAT3^{Y705} phosphorylation in multiple human cancer cell lines[24]. Treatment of PP tumor cells with LFM-A13 significantly decreased STAT3^{Y705} phosphorylation but did not affect AKT phosphorylation (Extended Data Fig. 8h). BMX-IN-1, a covalent BMX-selective inhibitor[25], similarly decreased phospho-STAT3^{Y705} levels with little effect on AKT phosphorylation (Extended Data Figure 8i). These findings suggest a model in which loss of PTEN results in enhanced PI3Kβ

signaling, leading to up-regulation of AKT and BMX-STAT3 signaling pathways, which promote oncogenic growth and immune evasion (Extended Data Fig. 8j).

Potential biomarkers of resistance

In order to investigate transcriptional changes upon PI3Kβ inhibition in models that more closely resemble a clinical setting, we used a panel of five patient-derived xenografts (PDXs) with various forms of PTEN deficiency (Extended Data Fig. 8k). Four models were derived from surgical resections of primary triple-negative breast cancer (TNBC), and one was derived from a metastatic lesion on the spine from a patient with ER+ disease (DFBC-1637). We treated PDX tumor-bearing NOG mice for four days with AZD6482 and harvested the tumors for RNA-Seq. GSEA of AZD6482 versus control for each PDX model revealed significant up-regulation of signatures of type I and II IFN signaling as well as antigen processing and presentation in three of the five models (DFBC-1510, DFBC-1637 and DFBC-1732) (Fig. 4a). To investigate potential mechanisms that could prevent up-regulation of immunogenic signatures upon PI3Kβ inhibition in the two resistant PDXs (DFBC-1613 and DFBC-1807), we compared the transcriptional profiles of each model (controls only) by GSEA. The results showed marked up-regulation of signatures associated with immune suppression in the two resistant models, including epithelial-to-mesenchymal transition (EMT), WNT, TGFβ and FGFR signaling[26–28], as well as up-regulation of signaling through the insulin and IGF1 receptors and KRAS (Fig. 4b), which have been shown to primarily activate PI3Kα signaling[7,29], and KRAS can also switch isoform dependence from PI3Kβ to PI3Kα in PTEN-null tumors[30]. Moreover, DFBC-1613 presented genomic amplification of the *IGF1R* gene (CNV = 4) and DFBC-1807 harbors a *PIK3CA^{H1047R}* oncogenic mutation on the PI3Kα gene, which could render further resistance to pharmacological inhibition of the PI3Kβ isoform.

PI3Kβ inhibition and immunotherapy

We then asked whether PI3Kβ-selective inhibition could stimulate immune responses and sensitize tumor cells to immune attack *in vivo*, and whether this treatment could benefit from combination with immune checkpoint blockade (ICB). First, we treated PP tumor-bearing FVB mice with AZD6482 for a short period of time and analyzed tumor response and T-cell activation by flow cytometry. AZD6482 treatment down-regulated P-AKT^{S473} and P-STAT3^{Y705} in PP tumor cells, and significantly enhanced CD4+ and CD8+ T-cell activation in the tumors (Extended Data Fig.9a). By stark contrast, AZD6482 treatment did not lead to any measurable change in AKT^{S473} or STAT3^{Y705} phosphorylation or T-cell activation in a syngeneic HER2/Neu+ mouse breast cancer model (Extended Data Fig. 9b) previously shown to require PI3Kα, but not PI3Kβ, for survival[31]. Next, we treated PP tumor-bearing mice with selective PI3Kα (BYL719) or PI3Kβ (AZD6482) inhibitors alone or in combination with PD-1 blockade. None of these agents administered as monotherapy affected tumor growth to a significant or consistent degree, and neither did combined treatment with BYL719 and ICB; on the other hand, AZD6482 combined with anti-PD-1 strongly synergized to inhibit tumor growth (Fig. 5a), consistently leading to complete response (CR) in up to 50% of cases (Fig. 5b). Histological analyses demonstrated complete absence of cancer cells in the residual tumor bed of fully regressed tumors, as well as

areas of enhanced immune infiltration and severe loss of tumor cellularity in cases showing delayed disease progression (Extended Data Fig. 9c). Consistently, short-term treatment with AZD6482 reduced AKT and STAT3 phosphorylation in tumor cells, which was not affected by PD-1 blockade, and enhanced T-cell activation, which was further enhanced in the combination treatment, particularly in terms of IFNγ production by CD8+ T-cells (Fig. 5c and Extended Data Fig. 9d–e). AZD6482 treatment also enhanced IFNγ production by inflammatory monocytes, which was not affected by addition of PD-1 blockade (Extended Data Fig. 9f). Transcriptome analyses of PP tumors harvested after four days of treatment showed that AZD6482 as a single agent enriched gene signatures and increased transcript levels of genes involved in immune response, which were significantly enhanced in the combination treatment with anti-PD-1 (Extended Data Fig. 9g–h).

We examined whether combined treatment conferred long-term immunity by re-challenging mice that showed CR to the combination treatment. Strikingly, re-challenged mice rejected PP tumors in 100% of cases, while no tumors were rejected in the control naïve mice (Fig. 5d). T-cell profiling of an independent cohort harvested two weeks after re-challenging, when tumors were still palpable, revealed enhanced T-cell infiltration and activation, reduced Treg levels, and markedly increased levels of memory T-cells in tumors from re-challenged mice, compared to tumors from control mice (Fig. 5e and Extended Data Fig. 10a). Changes in T-cell activation and memory T-cell levels in the draining lymph nodes (LNs) and spleens of the re-challenged mice were moderate (Extended Data Fig. 10b–c). These results suggest that local T-cell activation may play a major role in tissue-specific protection in this model.

Next, we evaluated our results in additional mouse models, including models with and without PTEN deficiency. First, we generated an isogenic pair of PTEN-WT and PTEN-deficient mouse mammary tumors by deleting *Pten* via CRISPR-Cas 9 in RCT-E302 mouse mammary tumor cells (Extended Data Fig. 11a), a syngeneic model previously developed by our lab[32]. Mice bearing RCT-E302 tumors with *Pten* deletion (RCT-E302-sgPten) or parental RCT-E302 tumors were treated with AZD6482. As predicted, AZD6482 treatment down-regulated AKT^{S473} and $STAT3^{Y705}$ phosphorylation in RCT-E302-sgPten tumor cells, and markedly enhanced CD4+ and CD8+ T-cell activation (Extended Data Fig. 11b). By contrast, inhibiting PI3Kβ did not affect AKT^{S473} and $STAT3^{Y705}$ phosphorylation or T-cell activation in parental RCT-E302 tumors (Extended Data Fig. 11c), indicating that loss of PTEN drives sensitivity to PI3Kβ inhibition-induced enhancement of T-cell activation in this model.

Next, we used a novel pair of syngeneic GEM models developed by injection of adenovirus expressing Cre recombinase directly into the lumen of mammary glands. The first model is driven by co-loss of *Brca1* and *Trp53* (designated BP[33]), and the second harbors additional homozygous *Pten* deletion (designated BPP; Extended Data Fig. 11d). Consistently, AZD6482 significantly reduced AKT^{S473} and $STAT3^{Y705}$ phosphorylation in BPP tumor cells and enhanced T-cell activation (Extended Data Fig. 11e). We did not detect significant changes in AKT^{S473} and $STAT3^{Y705}$ phosphorylation in BP tumor cells upon AZD6482 treatment; however, AZD6482 treatment led to a moderate enhancement of immune response, as evidenced by increased CD8+ T-cell IFNγ production (Extended Data

Fig. 11f), likely due to the connection between BRCA1 and PTEN in DNA damage and cancer[34].

We then evaluated the combination of PI3Kβ inhibition and PD-1 blockade in the BPP and RCT-E302-sgPten models. In both cases, AZD6482 significantly inhibited tumor growth, which was enhanced by anti-PD-1 (Extended Data Fig. 12a–b). Next, we evaluated PI3Kβ inhibition combined with immunotherapy in 4T1 mouse mammary tumors with *Pten* deletion by CRISPR-Cas9 (4T1-sgPten; Extended Data Fig. 12c). Of note, 4T1-sgPten tumors are characterized by markedly higher levels of M2-like macrophage polarization than the other three PTEN-null models (Extended Data Fig. 12d). M2-like TAMs associate with poor prognosis, can strongly induce immune suppression by directly and indirectly inhibiting T-cell cytotoxic and effector functions, and have been shown to render treatment resistance to various therapeutic agents[33,35,36]. We recently showed that pharmacological activation of STING enhanced innate and adaptive immune response by promoting DC activation and inducing reprograming of pro-tumorigenic M2-like TAMs to an anti-tumor M1-like phenotype, with a consequent enhancement of T-cell response[33]. Hence, for this model we evaluated the combination of AZD6482 with either PD-1 blockade or with the STING agonist MSA2. In this case, single arm treatments did not appreciably affect tumor growth, and neither did combined AZD6482 and anti-PD-1, while combined AZD6482 and MSA2 significantly reduced tumor growth (Extended Data Fig. 12e). This suggests that a highly immune suppressive macrophage population in 4T1-sgPten tumors may render resistance to PI3Kβ inhibition and overpower reinvigoration of T-cells by PD-1 blockade, and that reprograming TAMs via STING agonism synergizes with PI3Kβ inhibition. These results indicate that PI3Kβ inhibition may sensitize to different modalities of immunotherapy depending on the genomic context and nature of the immune infiltrate.

Discussion

The PI3K/AKT pathway is well recognized as one of the most important oncogenic nodes in breast cancer[11]. While the contributions of PI3K isoforms to cancer development have been described mostly in terms of promoting tumor cell-intrinsic mechanisms of survival and proliferation, our findings indicate that PI3Kβ-STAT3 signaling plays an important role in mediating immune evasion in the context of PTEN loss. Our results provide a molecular mechanism linking PTEN loss and STAT3 activation in cancer and cancer immune evasion, and are consistent with a previous study documenting the importance of tumor-intrinsic STAT3 in promoting immune evasion in a GEM model of PTEN-deficient prostate cancer[37]. Nevertheless, it has been shown that oncogenic AKT signaling can also contribute to immune evasion[38]. It is likely that the enhancement of immune response seen upon blocking PI3Kβ in PTEN-deficient breast tumors results from a combination of decreasing STAT3 signaling as well as other signaling pathways downstream of PI3Kβ, such as AKT. Interestingly, we also observed up-regulation of NF-κB signaling upon genetic or pharmacological PI3Kβ inactivation or upon Stat3 silencing. STAT3 has been shown to be a critical regulator of NF-κB[39]. These observations may be a consequence of changes in STAT3 activation that alter which transcriptional programs are induced by STAT3–NF-κB complexes. In addition, it has been shown that PI3Kγ inactivation in macrophages up-regulates NF-κB via increased IKKβ phosphorylation, which, together with concomitantly

decreased C/EBPβ, result in a shift towards an immune stimulatory phenotype[40]. It is possible that PI3Kβ could likewise regulate NF-κB activation in the context of PTEN loss.

Pharmacological targeting of the PI3K pathway is a major focus of anti-cancer drug development. AKT inhibitors have demonstrated significant clinical benefit both as single agents for patients harboring $AKT1^{E17K}$ mutations[41] and in combination with hormonal therapy[42]. The PI3Kα inhibitor alpelisib (BYL719) is approved for the treatment of HR+/HER2− advanced breast cancer harboring $PIK3CA$ mutations in combination with fulvestrant[43]. Nevertheless, progress has been hindered by significant adverse effects (AEs) and therapeutic resistance. A common AE of PI3Kα inhibitors is hyperglycemia, owing to the crucial role of PI3Kα in insulin signaling, and, notably, loss of PTEN is thought to confer clinical resistance to alpelisib[43,44]. Currently, PI3Kβ inhibitors are under clinical investigation for patients with PTEN deficiency or $PIK3CB$ mutations and have shown acceptable safety and tolerability profiles and preliminary efficacy in early clinical trials[45–48]. Indeed, specific targeting of PI3Kβ would allow a mechanism for achieving maximal inhibitory doses with few side effects, in part because PI3Kβ kinase activity does not play a significant role in insulin metabolism and glucose homeostasis[7,29]. In pre-clinical studies, combined PI3Kβ inhibition and ICB has shown positive responses in melanoma and prostate cancer models[6,49]. Together, our findings not only uncover the mechanism underlying PI3Kβ-dependent immune evasion in PTEN-null tumors, but also provide pre-clinical proof-of-concept for clinical development of PI3Kβ inhibition and its combination with immunotherapy in cancers with PTEN deficiency.

Online Content

Any methods, additional references, Nature Research reporting summaries, source data, extended data, supplementary information, acknowledgements, peer review information, details of author contributions and competing interests, and statements of data availability are available in the online version of the paper.

Methods

Mouse experiments.

Genetically-engineered mouse (GEM) models K14-Cre; $Pten^{L/L}$, K14-Cre; $Pten^{L/L}$; $Pik3ca^{L/L}$ and K14-Cre; $Pten^{L/L}$; $Pik3cb^{L/L}$ in FVB/NJ background have been described[10]. These mice were crossed with $Trp53^{L/L}$ to generate K14-Cre; $Pten^{L/L}$; $Trp53^{L/L}$ (PP), K14-Cre; $Pten^{L/L}$; $Trp53^{L/L}$; $Pik3ca^{L/L}$ (PPA) and K14-Cre; $Pten^{L/L}$; $Trp53^{L/L}$; $Pik3cb^{L/L}$ (PPB) GEM models. PP, PPA and PPB invasive breast cancer tumors were obtained by transplanting mammary tissue containing stem cells from PP, PPA or PPB GEMs into the cleared inguinal fat pad of a three-week-old nude mouse ($Foxn1^{nu}$; Jackson Laboratories). $Brca1^{L/L}$; $Trp53^{L/L}$ (BP) and $Brca1^{L/L}$; $Pten^{L/L}$; $Trp53^{L/L}$ (BPP) mice in FVB background (12 weeks old) were injected with adenovirus (2.5×10^7 PFU in 3 μL per injection) expressing Cre recombinase under a CMV promoter directly into the lumen of mammary glands to generate BP and BPP mammary tumors. RCT-E302 mouse mammary tumors in FVB background have been previously described[32]. HER2/Neu+ mouse mammary tumors in FVB background have been previously described[31,50]. $Rag1^{−/−}$

mice in the FVB background were a gift from Dr. Lisa Coussens (Oregon Health and Science University). Only female mice were used in this study. For all experiments involving tumor transplantations, 6–8-week-old mice were transplanted from single cell pools on the same day. For each cohort, equal numbers of tumor cells were injected orthotopically into the thoracic mammary fat pads in 40% matrigel. For experiments examining tumor growth *in vivo*, and for PD and immune profiling experiments, mice were transplanted with 1×10^6 tumor cells. For *in vivo* drug efficacy studies, mice were transplanted with 1×10^6 tumor cells (PP model) or 1×10^5 tumor cells (BPP, RCT-E302-sgPten and 4T1-sgPten models). Tumor growth was assessed by measuring the long and short axes with digital calipers, and tumor volume was calculated by use of the modified ellipsoid formula (long $\times$ short^2 $\times$ 0.52). The maximum tumor diameter permitted under the relevant animal protocols is 20 mm. Mice were monitored daily to avoid exceeding this limit. Any mouse inadvertently exceeding this limit was promptly euthanized. Other endpoints included ulceration or poor health, in which case mice were euthanized. For *in vivo* drug efficacy treatments of PP tumor-bearing mice, AZD6482 (80 mg/kg) and BYL719 (30 mg/kg) were dissolved in 10% 1-methyl-2-pyrrolidinone (NMP) and 90% polyethylene glycol 300 (PEG300) and administered daily by oral gavage. For *in vivo* drug efficacy treatments of BPP, RCT-E302-sgPten and 4T1-sgPten tumor-bearing mice, AZD6482 was dissolved in 7.5 NMP, 40% PEG400 and 52.5% ddH$_2$O and dosed at 60 mg/kg p.o. BID. This dosing regimen was also used for PD and immune profiling experiments. Anti-mouse PD-1 clone 332.8H3[51] was dosed at 250 μg per mouse every three days beginning on day 21 (PP) or day 5 (BPP, RCT-E302-sgPten and 4T1-sgPten) after tumor implantation and administered intraperitoneally (i.p.) for 2.5–4 weeks. MSA2 was dissolved in 5% DMSO, 95% PBS and dosed at 20 mg/kg every 5 days (BPP) or 3 times per week (E302-sgPten and 4T1-sgPten) for a total of 7 doses. For PD and immune profiling experiments, mice were treated for 3.5 or 10.5 days, respectively. Anti-mouse CD4 (clone GK1.5) and CD8 (clone YTS 169.4) depleting antibodies (Bio X Cell) were dosed at 400 μg per mouse, administered i.p. 48 and 24 hours prior to tumor transplantation, and then every four days. Sample sizes were determined based on previous experience with the models utilized, including experience in variability of tumor growth. For animal experiments evaluating pharmacological treatments, mice were randomized prior to start of treatment to ensure approximately equal initial mean tumor volume per condition. All tumor measurements within single cohorts were performed by the same researcher in order to avoid variation due to methodology. All drug treatments were performed by a researcher that was blinded to the analysis. All analyses were conducted by a second researcher. All mouse experiments were performed under institutional guidelines and approved by the Institutional Animal Care and Use Committee (IACUC) at Dana-Farber Cancer Institute (DFCI).

Mouse tissue dissociations.

To obtain single-cell suspensions for analysis by flow cytometry or scRNA-Seq, tumors were excised, minced and dissociated in collagenase/hyaluronidase buffer (10 mM HEPES, 5% FBS, 20 μg/mL DNase I [Stem Cell Technologies], 1X collagenase/hyaluronidase [Stem Cell Technologies]) for 45 minutes at 37 °C with agitation, followed by red blood cell (RBC) lysis (ACK Lysing Buffer [Lonza]), and strained through a 40 μm strainer for down-stream applications. To obtain single-cell suspensions for analysis of gene expression

in mouse tumors cells, tumors were excised, minced and dissociated in dispase buffer (4 U/mL dispase in Hank's balanced salt solution, 5% FBS, 20 μg/mL DNase I [Stem Cell Technologies], collagenase/hyaluronidase [Stem Cell Technologies] to 0.5X) for 35 minutes at 37 °C with agitation, followed by RBC lysis (ACK Lysing Buffer [Lonza]), and strained through a 40 μm strainer for tumor cell enrichment, which was performed by depleting CD45+ immune cells using EasySep mouse TIL (CD45) positive selection kit (Stem Cell Technologies) according to manufacturer's instructions. Spleens and lymph nodes were mechanically dissociated by passing through a 70 μm strainer, and RBCs were lyzed as above.

Patient-derived xenografts (PDXs).

Informed consent was obtained from patients with breast cancer who donated tumor tissue for this study. Patient tumor tissues from surgical resections or biopsies were transplanted into the mammary fat pad of NOG-F mice (NOD.Cg-*Prkdc^scid^ Il2rg^tm1sug^*/JicTac; Taconic). Tumors were allowed to grow in order to establish each model, and then propagated into more NOG-F mice for experimental studies. For this study, PDX-bearing NOG-F mice were treated with 90 mg/kg AZD6482 (p.o. BID) for 4 days (seven doses in total). Tumors were harvested two hours after the final dose and snap-frozen for RNA isolation and gene expression analysis as detailed below. All experiments were performed under institutional guidelines and approved by the Institutional Review Board (IRB) at the Dana-Farber/Harvard Cancer Center (DF/HCC) and IACUC at DFCI. Relevant clinical information is available on Supplementary Information Figure S21.

Tissue culture.

Primary mouse breast cancer cells (PP, PPA, PPB, BPP and BP) were isolated and grown by modifying a previously described protocol for primary tissue culture[52]. After dissociation from primary tumors, cells were initially grown at 37 °C in a humidified incubator under 5% CO_2 in F-Media (F12/DMEM (1:3) media (Gibco) supplemented with 25 ng/mL hydrocortisone (Sigma), 5 μg/mL insulin (Life Technologies), 8.5 ng/mL cholera toxin (Sigma), 0.125 ng/mL EGF (Sigma), 10 μg/mL gentamicin (Life Technologies) and 5 μM of the Rock1 inhibitor Y-27632 [Selleck]). After selection for cancer cells, cells were maintained in F-Media supplemented with 10% FBS (Gemini). HER2/Neu+ primary tumor cells were derived similarly, but using F12/DMEM (1:1) media supplemented with 0.6% FBS, 0.5 μg/mL hydrocortisone (Sigma), 10 μg/mL insulin (Life Technologies), 1.0 ng/mL cholera toxin (Sigma), 20 ng/mL EGF (Sigma), and 5 μM Y-27632 (Selleck). RCT-E302 and RCT-E302-sgPten cells were grown in RPMI 1640 media (Gibco) supplemented with 2% Tet-system approved FBS (Gibco). 4T1 and 4T1-sgPten cells were grown in RPMI 1640 media supplemented with 10% FBS. For *in vitro* proliferation assays, 1.0×10^4 cells were seeded in six-well plates in normal growth media and allowed to attach overnight. Media was replaced the next day with 80% Essential Minimum Eagle's Media (EMEM; ATCC) and 20% normal growth media. Cells were counted starting this day and every 24 hours. For *in vitro* drug treatments for characterizing PI3K isoform dependency in PP, PPA and PPB tumor cells, cells were treated with 1.0 μM PI3K inhibitors or DMSO as a control in normal growth media for 6 hours. For *in vitro* drug treatments of PP tumor cells for gene expression, western blot or ELISA analyses, 1.0×10^5 cells were seeded in 60 mm-diameter

culture dishes and allowed to attached overnight, serum-starved in EMEM without serum and supplemented with 5 μM Y-27632 overnight, and then treated with 5 μM AZD6482, 1.0 or 5.0 μM MK2206, 10 μM LFM-A13 or 10 μM BMX-IN-1 in serum-starvation conditions for 6 hours (western blots) or 72 hours (gene expression and ELISA). For *in vitro* treatment of human cancer cell lines, serum starvation and AZD6482 (5 μM) treatments were done in EMEM supplemented with 0.5% FBS. For *in vitro* treatments with IFNγ, cells were treated in normal growth media with 100 ng/mL IFNγ for 48 hours to measure MHC-I expression, and with 100 ng/mL or 1,000 ng/mL IFNγ for 72 hours to measure cell viability. Cell viability was measured by CellTiter-Glo Luminescent cell viability assay (Promega) according to manufacturer's instructions. Human cell lines (HEK-293T, # CRL-3216; BT549, # HTB-122; HCC70, # CRL-2315; MDA-MB-436, # HTB-130; MDA-MB-468, # HTB-132) and 4T1(# CRL-2539) mouse cell line were obtained from ATCC. Human cell lines were authenticated via STR analysis. 4T1 cells were used as early passage and were not authenticated. Cells were not tested for mycoplasma.

Plasmid transfections, viral infections, RNA interference and CRISPR-Cas9 gene editing.

Lentiviral-based mouse PI3Kβ in pReceiver-Lv242-puro backbone (clone Ex-Mm35124-Lv242) was obtained from GeneCopoeia. Lentiviral-based shRNA against mouse *Stat3* in pLKO.1puro backbones (TRCN0000071456 [#1; target sequence: CCTGAGTTGAATTATCAGCTT] and TRCN0000071453 [#2; target sequence: CCTAACTTTGTGGTTCCAGAT]) were obtained from SigmaAldrich. Lentivirus were amplified by transfecting HEK-293T cells with 1.2 μg each of Gag/Pol, Tat and Env, 2.4 μg Vsv-g packaging plasmids, and 24 μg of the lentiviral expression plasmid using TransIT (Mirus). Supernatants containing virus were collected and filtered after 48 hours. Murine pMXs-STAT3[A661C,N663C] was purchased from Addgene (#13373)[53]. Retrovirus were amplified by transfecting HEK-293T cells with 4.0 μg pMD.MLV and 1.4 μg pMD.G packaging plasmids, and 5.4 μg of the retroviral expression plasmid using Lipofectamine 3000 (ThermoFisher) according to manufacturer's instructions. For CRISPR-Cas9 gene editing, tumor cells were transiently transfected with double nickase plasmids encoding gRNA (sc-422475; A: TCTGTGAAGATCTTGACCAA; B: GGTTTGATAAGTTCTAGCTG) and Cas9n (D10A nickase mutant), as well as a puroR and GFP as selection markers. Transfected cells were selected by GFP+ sorting followed by puromycin resistance. Efficiency of gene deletion was assessed by western blotting. For 4T1-sgPten, selection of a single clone with efficient *Pten* deletion was necessary. For RCT-E302-sgPten, single clone selection was not necessary.

Histology.

For histology analyses, formalin-fixed tissue sections were embedded in paraffin, sectioned, and stained with hematoxylin and eosin (H&E) by the DF/HCC Rodent Histopathology Core. Histological classification was done by a qualified rodent histopathologist at the DF/HCC Rodent Histopathology Core. For immunohistochemistry (IHC), diaminobenzidine (DAB) staining was performed according to standard protocols using DAB EnVision+ System (Dako) on formalin-fixed paraffin-embedded (FFPE) sections and visualized under a brightfield microscope. Briefly, 5 μm-thick sections were deparaffinized with xylene, followed by gradation washes in 100%, 95% and 80% ethanol before heat-induced antigen

retrieval in 10 mM sodium citrate buffer (pH 6.0) for 20 min in a steamer. Sections were then treated with peroxidase block (Dako) for 10 min and incubated overnight at 4 °C with primary antibody (PTEN [1:100 dilution]; CST #9559).

Immunofluorescent microscopy.

Tissue-based cyclic immunofluorescence (CyCIF) was carried out as previously described[54]. Briefly, tumors were fixed in formalin and embedded in paraffin. 5 μm sections were cut and mounted on positively charged glass slides. Each tumor section underwent dewaxing and antigen retrieval on Bond Rx automated stainer (Leica). In the first round, sections were incubated with unconjugated antibodies and then labelled with secondary fluorophores. Sections then underwent sequential incubation with fluorophore-conjugated antibodies. Antibodies and dilutions used can be found in Supplementary Information Table S15. In each round, antibodies were incubated overnight followed by imaging using InCell Analyzer 2200 (GE Technologies). For each section, a region of interest was defined for the first cycle of imaging and subsequently used for every subsequent cycle without alteration. Sections were bleached before incubating with the next round of antibodies. After imaging was completed, each tile was assembled into a multi-field composite image using ASHLAR and BaSiC as previously described[54]. The same sections used for tCyCIF were stained with H&E and imaged on a light microscope.

Flow cytometry.

Tissue was dissociated as described above to obtain single cell suspensions. One million cells were labeled with Live-Dead Fixable Aqua Dead Cell Stain (Life Technologies) and blocked with anti-mouse CD16/32 (Biolegend). Cells were fixed and permeabilized using Foxp3/Transcription Factor Staining Buffer Set (eBioscience) according to manufacturer's instructions. For intracellular cytokine analyses, cells were stimulated with Leukocyte Activation Cocktail (BD Biosciences) according to manufacturer's instructions. Antibodies used in this study can be found in Supplementary Information Table S16. Flow cytometry was performed on an LSR Fortessa HTS instrument (BD Biosciences) and collected using FACSDiva (BD Bioscience), and all data were analyzed using FlowJo. Sample sizes are shown on each graph. Gating strategies can be found in Supplementary Information Figs. S10–S20.

Single-cell RNA sequencing (scRNA-Seq).

Single-cell RNA-Seq was performed using the Seq-Well platform[55] to capture transcriptomes of single cells on barcoded mRNA capture beads; full methods on implementation of this platform are available. Briefly, single-cell suspensions were prepared from tumors five days post-injection in PP, PPA, and PPB mice (n = 3 each), as described above. The cells in suspension were stained with CD45-FITC, CD3-PE/Dazzle594 and 7-AAD, sequentially gated on live cells, CD45 and CD3, and sorted using a BD FACSAria II high-speed sorter (BD Biosciences). 8,000 cells from the CD45+, CD3− gate and 8,000 cells from the CD45+, CD3+ gate were co-loaded onto a Seq-Well array preloaded with barcoded mRNA capture beads (ChemGenes). A selectively permeable polycarbonate membrane was used to seal individual wells on the array to allow for isolated single-cell lysis and transcript hybridization. Each library was then treated with Exonuclease I (NewEngland

Biolabs M0293L) to remove excess primers. To increase transcript recovery, cDNA was amplified with second strand synthesis[56] before PCR amplification using KAPA HiFi PCR Mastermix (Kapa Biosystems KK2602). Final cDNA libraries were constructed using the Nextera XT DNA tagmentation method (Illumina FC-131–1096). Tagmented and amplified cDNA libraries were subsequently purified and sequenced using an Illumina 75 Cycle NextSeq500–500v2 kit (read1: 20 12 bp barcode, 8 bp UMI; read2: 50).

Single-cell RNA-seq alignment and analysis.

Read alignment was performed as previously described[57]. Briefly, for each NextSeq sequencing run, raw sequencing data was converted to demultiplexed FASTQ files using bcl2fastq2 based on Nextera700 indices corresponding to individual samples/arrays. Reads were then aligned to the mm10 genome using the Galaxy portal maintained by the Broad Institute for Drop-Seq alignment. Individual reads were tagged according to the 12 bp cell barcode and the 8 bp UMI contained in Read 1 of each fragment. Following alignment, reads were binned onto 12-bp cell barcodes, and collapsed by their 8-bp UMI. Digital gene expression matrices for each array were obtained from quality filtered and mapped reads, with an automatically determined threshold for cell count. To retain high-quality cells for downstream analysis, we performed thresholding of cells based on UMI detection (>500), number of genes identified (>200), and housekeeping gene expression (>0.4 average expression). The filtered gene expression matrix was loaded into a Seurat object[58], and log-normalized and scaled. To perform dimensionality reduction and clustering analysis, 450 variable genes with scaled expression value >0.3 and dispersion >1.0 were first selected using the FindVariableGenes function in Seurat. Principal Component Analysis (PCA) was performed on this list of variable genes and all cells, and the top significant principal components were determined using the PCElbowPlot function in Seurat. Significant PCs were used for t-stochastic neighbor embedding (t-SNE), and significant clusters from kmeans clustering were identified by the Seurat FindClusters function. To identify genes defining each cluster, we performed a ROC test implemented in Seurat with a threshold set to AOC = 0.7. Top marker genes were used to classify cell clusters into cell types, using the ImmGen mouse immune gene expression database (immgen.org) for reference. Cell clusters were then subset into individual Seurat objects and sub-clustered to increase resolution of differences in cell-type gene expression between genotypes.

Ex vivo co-culture.

For tumor cell/CD8+ T cell co-culture, CD8+ T-cells were isolated from the spleens of FVB mice using EasySep Mouse CD8+ T Cell Isolation Kit (Stem Cell Technologies) according to manufacturer's indications. 1.0×10^5 T-cells were co-cultured with tumor cells at 1:2 and 1:4 ratios (tumor cells : T-cells) in T-cell media (RPMI 1640 containing 2.5 ng/mL IL-7 [PeproTech], 50 ng/mL IL-15 [PeproTech], 2 ng/mL IL-2 [PeproTech], 55 µM 2-mercaptoethanol [Gibco] and 10% FBS [Gemini]). Two days after co-culture, T-cells were analyzed by flow cytometry as described above. For tumor cell/dendritic cell (DC) co-cultures, we derived DCs from the bone marrow of naïve FVB mice by flushing the tibiae and femurs, and collecting the eluate containing hematopoietic progenitor cells. Cell suspensions were washed, RBCs were lysed as above, and cells were plated at a density of 2×10^6 viable cells per plate in RPMI 1640 complete media supplemented with 150

ng/mL FLT-3L (Preprotech). Media was replaced after three days. On day five, non-adherent cells (enriched for bone marrow-derived dendritic cell [BMDC] fraction) were collected. To set up the co-culture, tumor cells were seeded onto 6-well plates (5×10^4 cells in 500 μL media for each well) and allowed to adhere overnight. On the second day, 5×10^4 BMDCs in 500 μl media were added onto tumor cells and co-cultured overnight. BMDC activation was analyzed by flow cytometry. For triple co-culture of tumor cells, BMDCs and T-cells, tumor cells and BMDCs were first co-cultured as described above for two days. Then, BMDCs were collected and transferred into co-cultures with freshly isolated CD8+ T-cells at 1:24 ratios (BMDCs : T-cells) in T-cell media for 16 hours. T-cells were then analyzed by flow cytometry as above. For tumor cell/bone marrow-derived cell (BMC) co-cultures, hematopoietic progenitor cells were obtained from mouse tibiae and femurs as above. To set up the co-culture, tumor cells were seeded onto 6-well plates (5×10^4 cells in 500 μL media for each well) and allowed to adhere overnight. BMCs were plated (5×10^4 BMCs in 500 μl media) on top of tumor cells in RPMI 1640 complete media without supplements (i.e. without exogenously added FLT-3L or GM-CSF). Non-adherent cells were collected after five days for analysis by flow cytometry.

Western blotting.

Cells were lysed in EBC_{250} buffer (250 mM NaCl, 50 mM Tris pH 8.0, 0.5% NP40, 50 mM NaF) supplemented with Halt™ Phosphatase Inhibitor (Thermo Scientific) and cOmplete™ Mini EDTA-free protease inhibitor cocktail (Roche). Proteins were resolved by SDS-PAGE and transferred to polyvinylidene fluoride (PVDF) membranes, and hybridized to primary antibodies and fluorescently labeled secondary antibodies for detection by Odyssey CLx imaging system (Li-Cor). Primary and secondary antibodies and antibody dilutions used in this study can be found in Supplementary Information Table S17. Uncropped immunoblots are available on Supplementary Information Figs. S22–S25.

Gene expression analyses.

For analysis of gene expression in mouse tumor cells grown as monolayer *in vitro*, total RNA was isolated using RNeasy Plus Mini Kit (Qiagen) for analysis by Q-PCR or transcriptome profiling as detailed below. For analysis of gene expression in mouse tumor cells isolated from tumors *in vivo*, tumors were first dissociated with dispase buffer and enriched for tumor cells as detailed above. Total RNA from enriched tumor cells was extracted using RNeasy Plus Micro Kit (Qiagen) for mouse-specific transcriptome analysis as detailed below. For quantitative PCR (Q-PCR), cDNA was synthesized from total RNA by reverse transcription using SuperScript III First-Strand Synthesis System (Invitrogen). Q-PCR was performed in a 7300 Real-Time PCR System (Applied Biosystems) using QuantiTect SYBR Green PCR Kit (Qiagen) according to manufacturer's instructions. Mouse-specific transcriptome analysis and gene set enrichment analysis (GSEA) were performed as previously described[59]. Briefly, RNA was sequenced on an Ion Torrent Proton platform (Thermo Fisher) using a mouse-specific Ion AmpliSeq Custom Panel designed to target 4,604 cancer and immunology-related genes. Multiple libraries were amplified using an Ion OneTouch 2 System (Thermo Fisher). Raw and normalized count data were generated using Torrent Suite and AmpliSeqRNA analysis plugin (Thermo Fisher). For network analyses of mouse transcriptome, we used Ingenuity Pathway Analysis

(IPA) software (Qiagen Inc., https://digitalinsights.qiagen.com/IPA) based on the Ingenuity Knowledge Base[60]. For GSEA[61] of mouse transcriptome, we used the MSigDB Hallmarks v6.1 dataset with weighted enrichment statistic and signal-to-noise metric for ranking genes, and 1,000 permutations. For gene expression analysis of human PDX samples, total RNA was extracted using RNeasy Plus Mini Kit (Qiagen). Frozen PDX fragments were lyzed using polypropylene pellet pestles and a cordless motor. RNA-Seq was performed by Novogene using their NovaSeq PE150 pipeline. For GSEA of human transcriptome, we used the MSigDB Hallmarks v2022.1, Gene Ontology v2022.1, Reactome v2022.1, wikipathways v2022.1 and Oncogenic Signatures v2022.1 datasets with weighted enrichment statistic and signal-to-noise metric for ranking genes, and 1,000 permutations. Gene overlaps for IPA and GSEA are available on Supplementary Information Tables S1–S14. The cBio Portal for Cancer Genomics[62,63] was used for analysis and visualization of genetic alterations on *PTEN* and *TP53* using data from The Cancer Genome Atlas (TCGA).

ELISA.

To measure secreted GM-CSF or IL-6, 1×10^5 primary tumor cells were seeded in 60 mm-diameter culture dishes and were allowed to attach overnight. Cells were then starved in serum-free EMEM, and supernatants were collected after 72 hours for analysis using mouse GM-CSF ELISA kit (Invitrogen) or mouse IL-6 ELISA kit (Invitrogen) according to manufacturer's instructions.

Statistical analyses.

Statistical comparisons of mean values and survival curves was performed using GraphPad Prism version 9 for Mac OS (GraphPad Software, San Diego, CA USA, www.graphpad.com). For comparison of two means, unpaired, two-tail t-test with Welch's correction assuming unequal variance. For multiple comparisons, one-way ANOVA followed by Tukey's multiple comparisons tests. For comparison of survival curves, log-rank (Mantel-Cox) test. All measurements were taken from distinct samples.

Extended Data
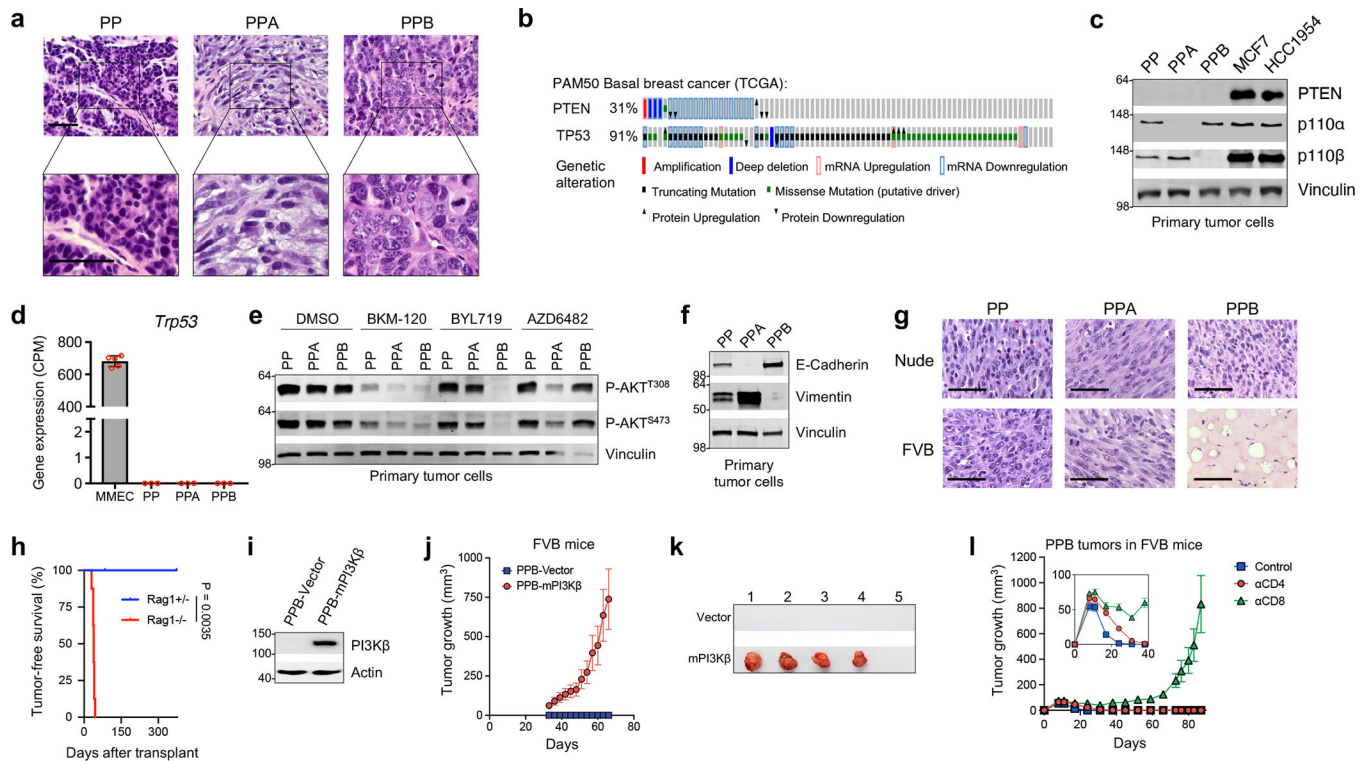
**Extended Data Figure 1 |. Characterization of breast cancer GEM models.**
a, H&E staining of primary PP (n = 4), PPA (n = 3) and PPB (n = 4) tumors. Representative images shown. **b**, Genetic alterations in *PTEN* and *TP53* in patient samples of PAM50 basal breast cancer from The Cancer Genome Atlas (TCGA). **c-e**, Characterization of PP, PPA and PPB primary tumor cells by western blotting (**c**) and RNA-Seq (**d**; n = 5 biological replicates for MMEC; n = 3 biological replicates for PP, PPA and PPB), compared to positive controls for PTEN (MCF7 and HCC1954) and *Trp53* (mouse mammary epithelial cells; MMEC). Data in (**d**) presented as mean values and s.d. **e**, Tumor cells were treated with 1.0 μM pan-PI3K inhibitor (BKM-120), PI3Kα inhibitor (BYL719) or PI3Kβ inhibitor (AZD6482) for one hour in complete growth media containing 10% FBS. Whole-cell lysates were analyzed by western blotting. Immunoblot representative of two independent experiments. **f**, Western blot analysis of primary tumor cells. Immunoblot representative of three independent experiments. **g**, H&E staining of transplanted tumors or remaining tumor bed from nude and FVB mice. Scale bars = 100 μm. Representative images shown (nude; PP, n = 8 tumors; PPA and PPB, n = 4 tumors; FVB, n = 8 tumors per group). **h**, Tumor-free survival of $Rag1^{+/-}$ (n = 4 mice) and $Rag1^{-/-}$ (n = 8 mice) FVB mice injected with PPB tumor cells. Statistical analysis by Log-rank (Mantel-Cox) test. **i-k**, PPB tumor cells were stably transfected with a vector control or mouse PI3Kβ. **i**, Western blot analysis. **j**, Tumor growth in immunocompetent syngeneic FVB mice (n = 5 tumors per group). Data presented as mean values and s.e.m. **k**, Tumors after necropsy. **l**, PPB tumor volume after transplanting into FVB mice treated with or without CD4 or CD8 depleting antibodies (n = 10 tumors per

group). Inset shows magnified view of early time points. Data presented as mean values and s.e.m. Apparent molecular weights in kDa are indicated for immunoblots.
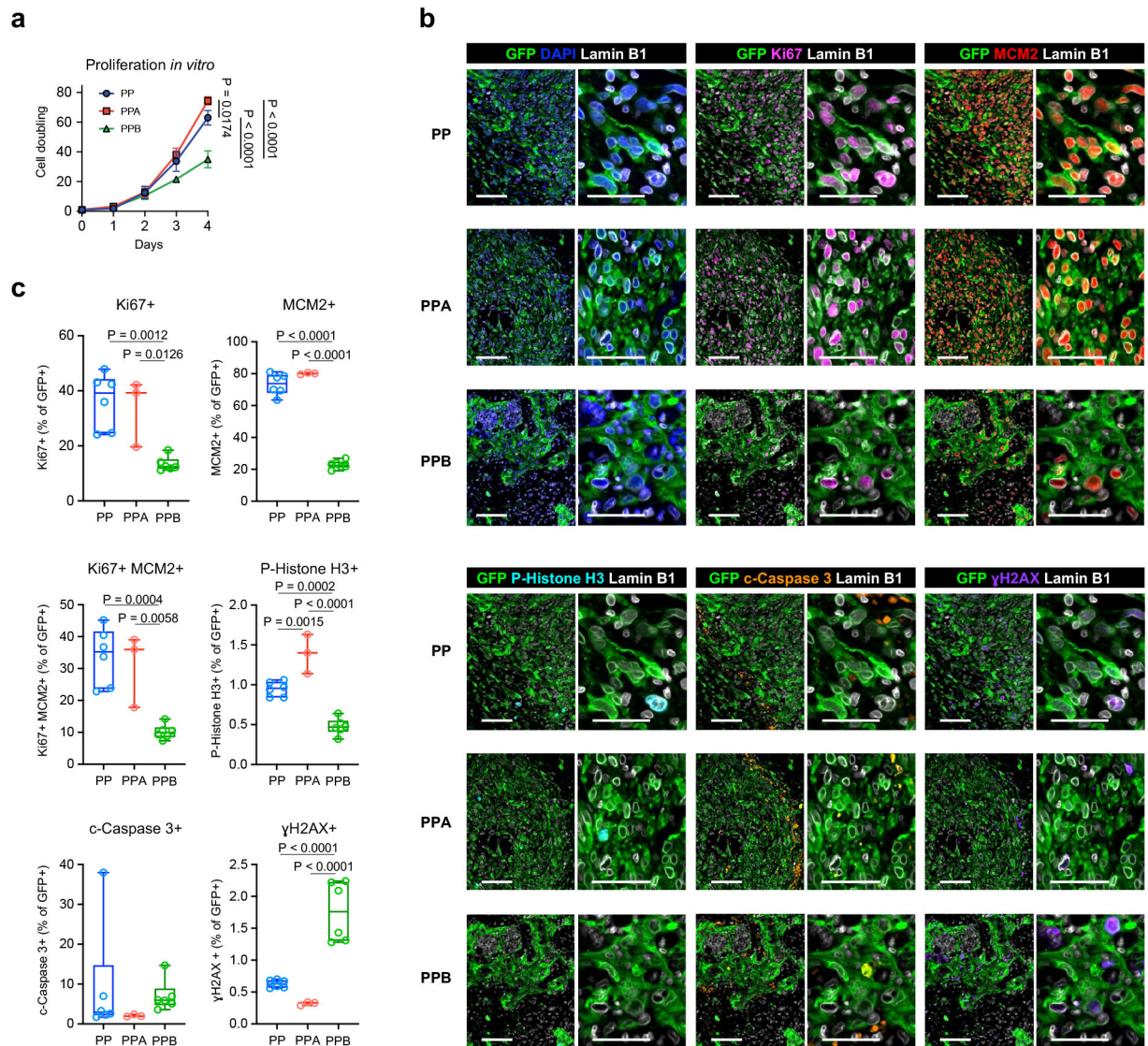

Extended Data Figure 2 |. PPB tumor cells exhibit reduced levels of proliferation *in vitro* and *in vivo*.

a, Cell proliferation *in vitro* under reduced serum/nutrient conditions. Data shown as mean and s.d. (n = 6 biological replicates per condition). **b-c**, Analysis of GFP-tagged PP, PPA and PPB tumors harvested five days after tumor cell transplantation into nude mice. Representative sections (**b**) and quantification (**c**) are shown (n = 6 tumors for PP and PPB; n = 3 tumors for PPA). GFP was added via lentiviral transduction *in vitro* prior to transplantations. Scale bars: 100 μm (left) and 50 μm (right). Box plots represent median and inter-quartile range, and min-to-max error bars (whiskers). For comparison of multiple mean values (**a** and **c**), one-way ANOVA followed by Tukey's multiple comparisons tests.
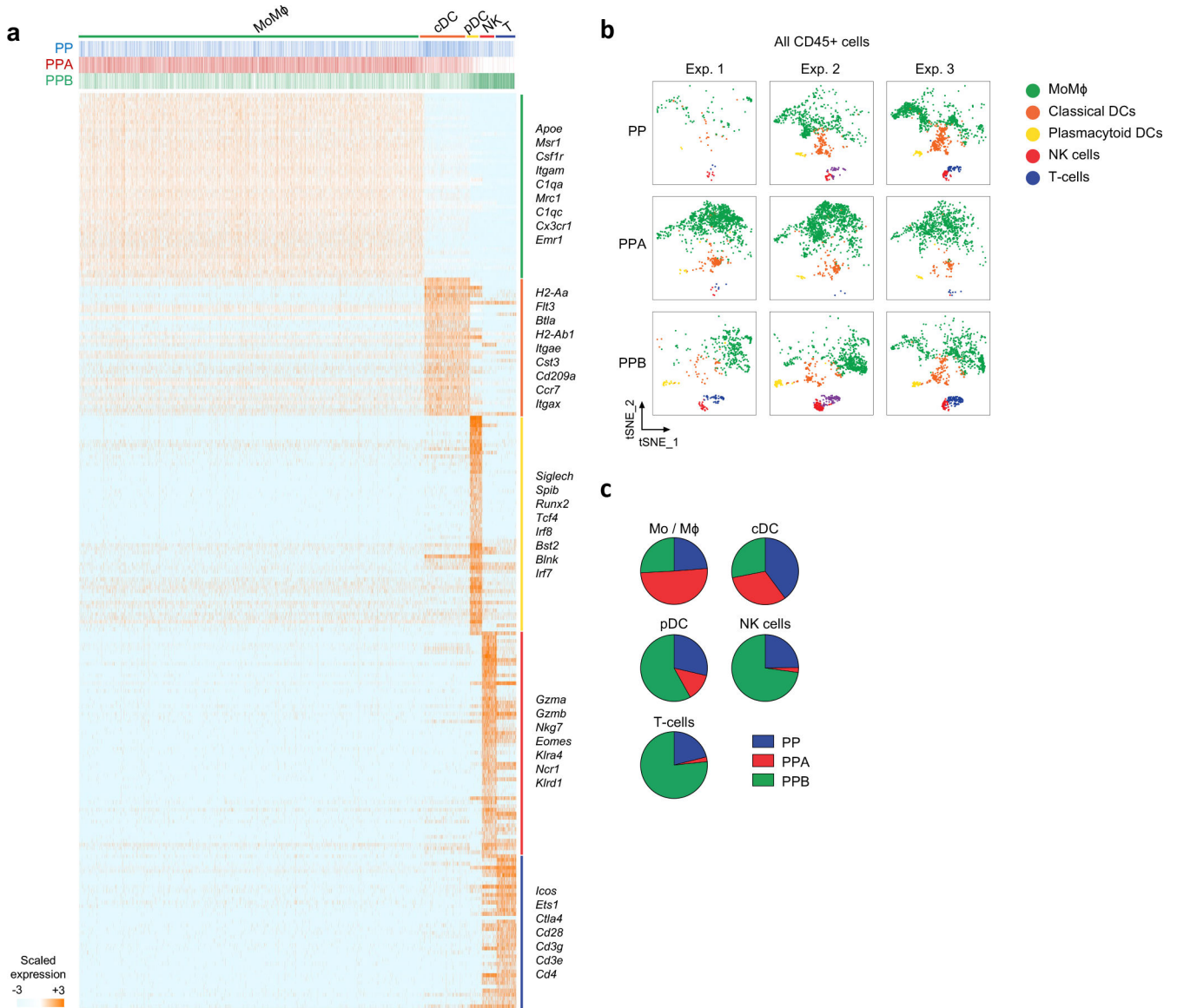
Extended Data Figure 3 |. Single-cell RNA-Seq analysis of immune infiltrate in PTEN/p53-null breast tumors with catalytic isoform-specific PI3K deletion.

Single-cell RNA-Seq (scRNA-Seq) analysis of immune infiltrate from PP, PPA and PPB tumors (n = 3 mice per group). Tumors were harvested and dissociated into single cells, followed by FACS sorting for viable immune (CD45+) cells prior to scRNA-Seq analysis via Seq-Well technology. **a**, Heatmap showing gene expression for top 10% differentially-expressed genes (DEGs) for each cell type cluster. Selected genes for each cluster are indicated on the right. Genotype of the tumor of origin is indicated on top. **b**, tSNE of all CD45+ cells analyzed denoting experimental replicate and cell type. **c**, Genotype representation per cell type. Complete list of DEGs per cell type is available in the source data linked to this article.
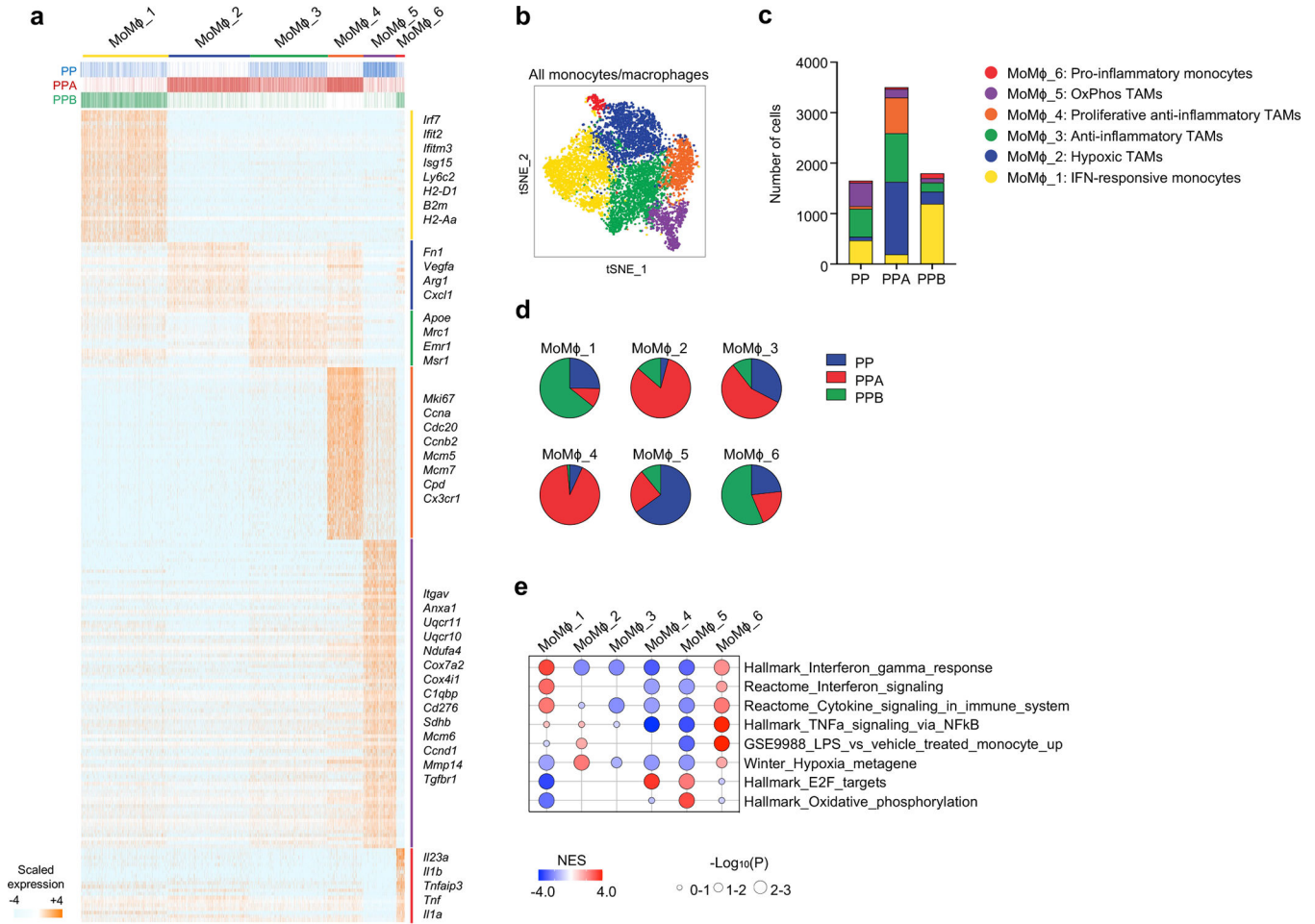
Extended Data Figure 4 |. Single-cell RNA-Seq analysis of monocytes/macrophages cluster in PTEN/p53-null breast tumors with catalytic isoform-specific PI3K deletion.
Single-cell RNA-Seq analysis of monocytes/macrophages (MoMφ) cluster from PP, PPA and PPB tumors (n = 3 mice per group). **a**, Heatmap showing gene expression for top 10% differentially-expressed genes (DEGs) for each MoMφ sub-cluster. Selected genes are indicated on the right. Genotype of the tumor of origin is indicated on top. **b**, tSNE of all MoMφ analyzed denoting sub-cluster. **c**, MoMφ sub-cluster representation per genotype. **d**, Genotype representation per MoMφ sub-cluster. **e**, GSEA of MoMφ sub-clusters. Statistical significance of enrichment scores (p-values) were calculated by GSEA using a phenotype-based permutation test. Complete list of DEGs per MoMφ sub-cluster is available in the source data linked to this article.
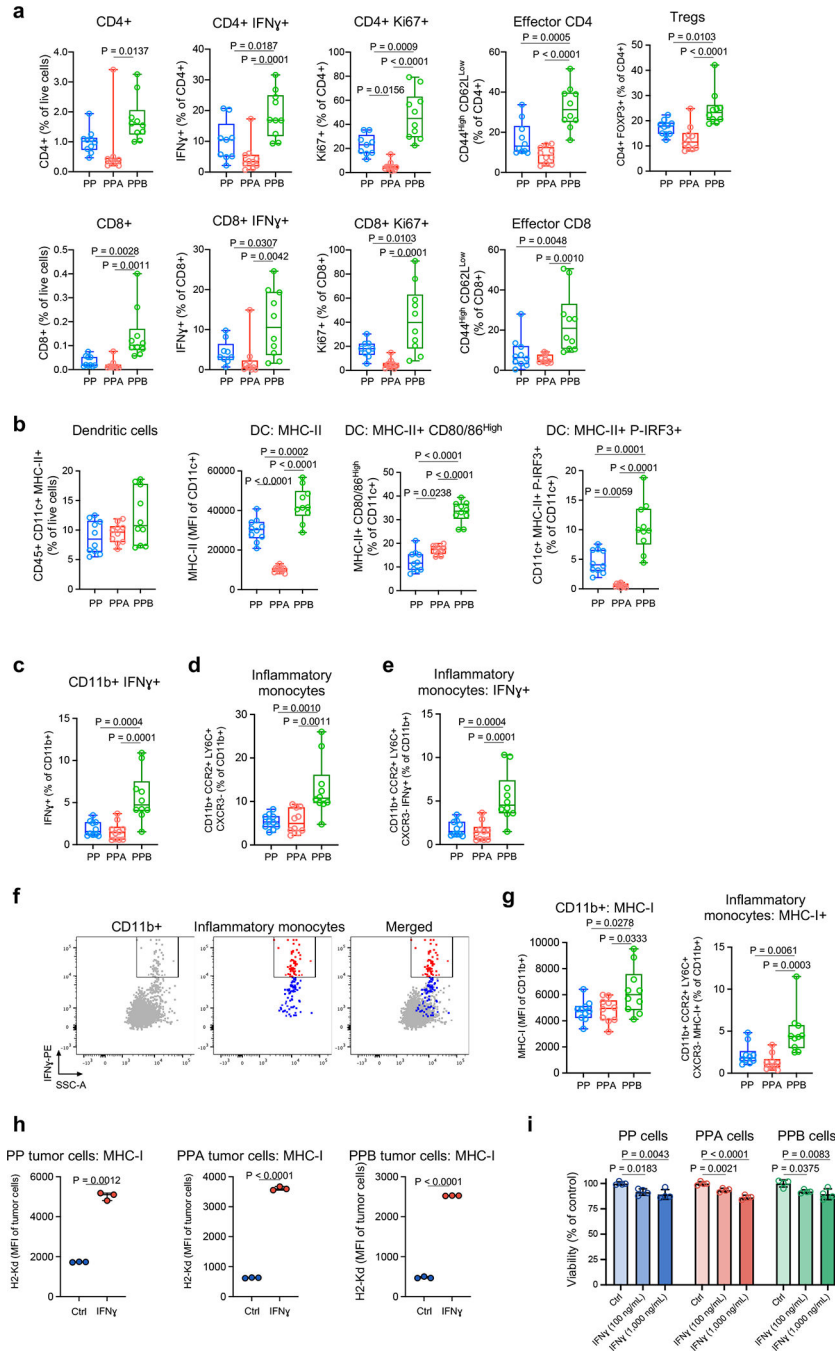
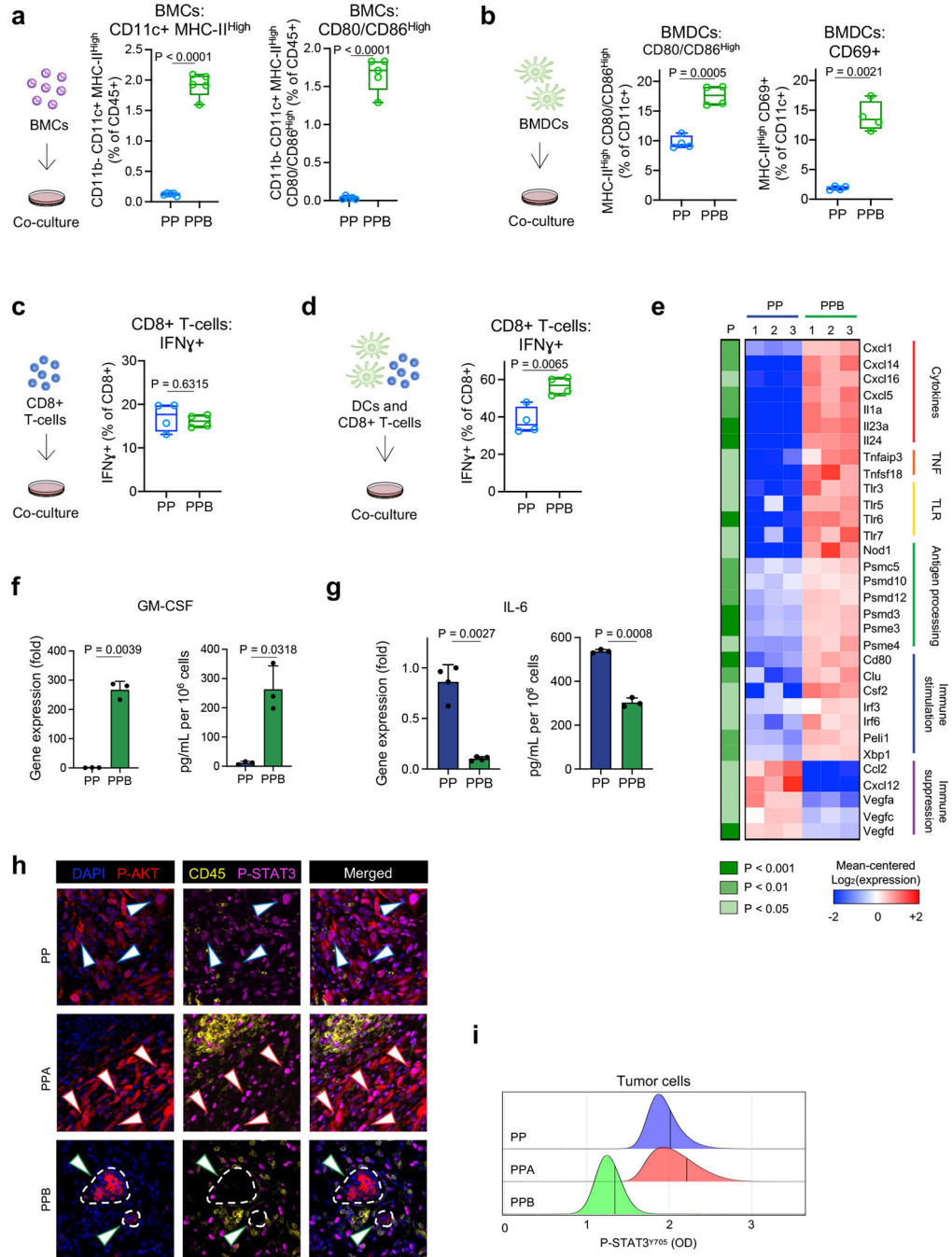**Extended Data Figure 5 |. Enhanced immune cell activation in PPB tumors.**

a-g, Flow cytometry analysis of PP, PPA and PPB tumors harvested five days after tumor cell transplantation into FVB mice (n = 10 tumors per group). Box plots represent median and inter-quartile range, and min-to-max error bars (whiskers). Representative gating profiles to demonstrate that myeloid-derived IFNγ is primarily produced by inflammatory monocytes are shown on (**f**). **h**, PP, PPA and PPB tumor cells were treated with 100 ng/mL IFNγ *in vitro* for 48 hours. MHC class I (MHC-I) expression was analyzed by flow cytometry (n = 3 biological replicates per condition). Data shown as median and min-to-max

error bars. **i**, PP, PPA and PPB tumor cells were treated with IFNγ *in vitro* for 72 hours. Cell viability was analyzed by CellTiter-Glo. Data shown as mean values and s.d. (n = 4 biological replicates per condition). For comparison of two means (**h**), unpaired, two-tail t-test with Welch's correction assuming unequal variance. For multiple comparisons (**a-e, g** and **i**), one-way ANOVA followed by Tukey's multiple comparisons tests. Flow cytometry gating profiles available on SI Fig. S1.

Extended Data Figure 6 |. PPB tumor cells enhance immune cell activation *ex vivo*, and show enhanced inflammatory signaling and reduced STAT3 pathway activation.

a-d, Flow cytometry analyses of immune cells from co-culture experiments *ex vivo*. **a**, Analysis of bone marrow-derived cells (BMCs) co-cultured with tumor cells (n = 5 biological replicates per group). **b**, Analysis of bone marrow-derived dendritic cells (BMDCs) co-cultured with tumor cells (n = 4 biological replicates per group). **c**, Analysis of CD8+ T-cells co-cultured with tumor cells (n = 4 biological replicates per group). **d**, Analysis of CD8+ T-cells co-cultured with dendritic cells (DCs) that had previously been co-cultured with tumor cells (n = 4 biological replicates per group). Box plots represent median and inter-quartile range, and min-to-max error bars (whiskers). Flow cytometry gating profiles available on SI Fig. S2. **e**, Heatmap of gene expression for immune-related genes in primary tumor cells (n = 3 biological replicates per group). **f**, Analysis by Q-PCR (left) and ELISA (right) of GM-CSF expression by PP and PPB cells. Data presented as mean values and s.d. (n = 3 biological replicates per group). **g**, Analysis by Q-PCR (left; n = 4 biological replicates per group) and ELISA (right; n = 3 biological replicates per group) of IL-6 expression by PP and PPB cells. Data presented as mean values and s.d. **h-i**, Immunofluorescence analysis of PP, PPA and PPB tumors harvested five days after tumor cell transplantation into FVB mice, including representative sections (**h**; n = 3 tumors per group) and quantification of STAT3^{Y705} phosphorylation in tumor cells as assessed by fluorescence intensity (**i**). Results correspond to further analysis of samples in Fig. 2a. Tumor cells show positive P-AKT staining (red color). Blue and red-lined arrows point to examples of PP and PPA tumor cells with high P-STAT3. Green-lined arrows point to PPB tumor cell clusters highlighted with white dashed line. For comparison of two means (**a-g**), unpaired, two-tail t-test with Welch's correction assuming unequal variance. OD, optical density; TNF, tumor necrosis factor; TLR, toll-like receptor.
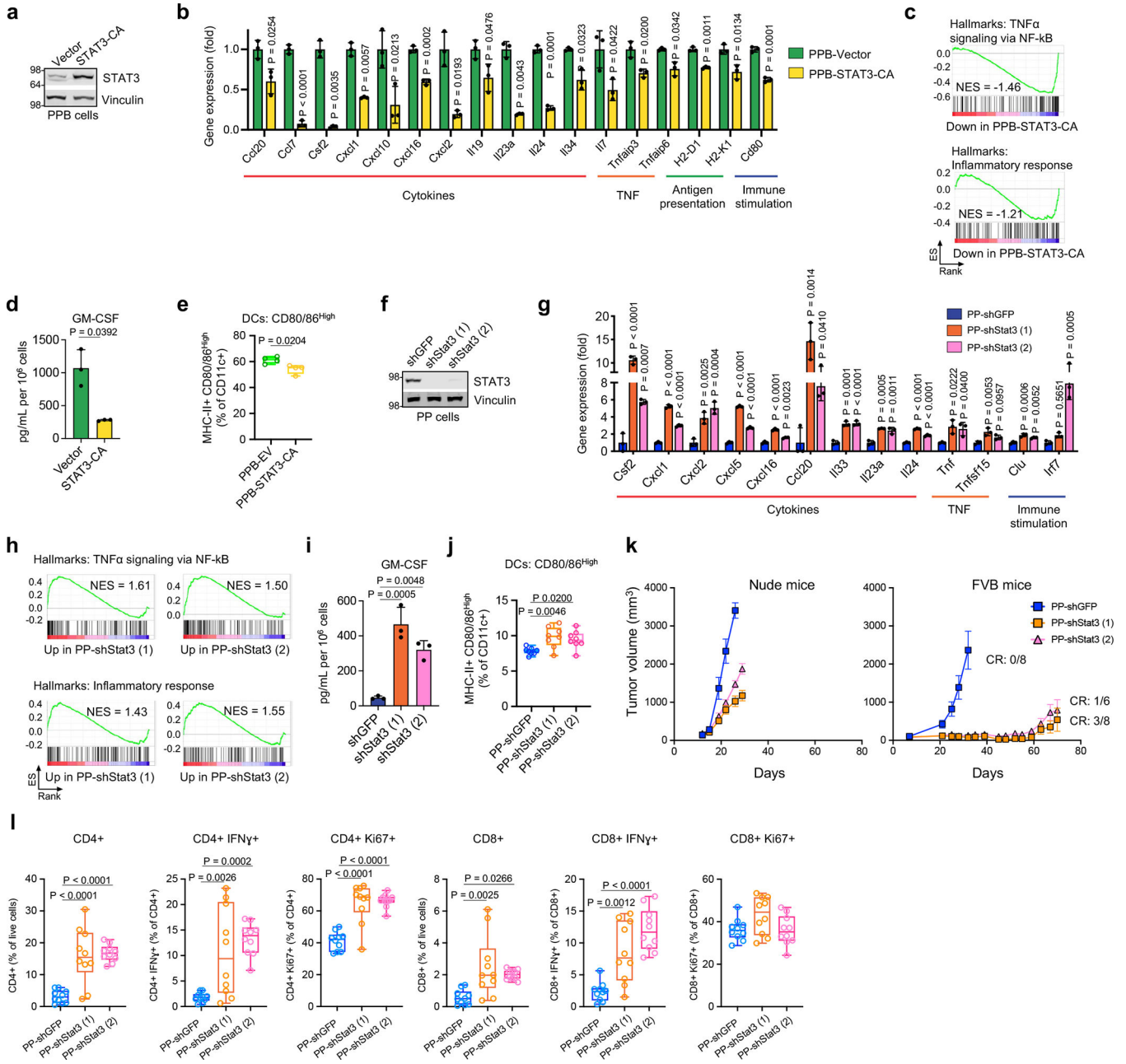
Extended Data Figure 7 |. The PI3Kβ-STAT3 pathway mediates immune suppressive signaling in PTEN/p53-null breast tumor cells.

a-d, Analysis of PPB cells stably expressing an empty vector control (vector) or constitutively-active STAT3$^{A661C, N663C}$ (STAT3-CA) by western blotting (**a**), gene expression (**b**; n = 3 biological replicates per group), GSEA (**c**; n = 3 biological replicates per group), and ELISA (**d**; n = 3 biological replicates per group). **e**, Flow cytometry analysis of dendritic cells (DCs) co-cultured with tumor cells (n = 4 biological replicates per group). **f-i**, Analysis of PP cells transduced with shRNA against GFP (shGFP) or Stat3 (shStat3; two independent constructs) by western blotting (**f**), gene expression (**g**; n = 3 biological replicates per group), GSEA (**h**; n = 3 biological replicates per group), and ELISA (**i**; n = 3

per group). **j**, Flow cytometry analysis of DCs co-cultured with tumor cells (n = 8 biological replicates per group). **k**, Tumor volume after transplantation into immunodeficient mice (nude; n = 10 tumors per group) or syngeneic immunocompetent mice (FVB; n = 8 tumors for PP-shGFP and PP-shStat3(1); n = 6 tumors for PP-shStat3(2)). Data presented as mean values and s.e.m. **l**, Flow cytometry analysis of immune infiltrate after tumor transplantation into FVB mice. Apparent molecular weights in kDa are indicated for immunoblots. Data on (**b**), (**d**), (**g**) and (**i**) are presented as mean values and s.d. Box plots represent median and inter-quartile range, and min-to-max error bars (whiskers). For comparison of two means (**b, d-e**), unpaired, two-tail t-test with Welch's correction assuming unequal variance. For multiple comparisons (**g, i, j** and **l**), one-way ANOVA followed by Tukey's multiple comparisons tests. Flow cytometry gating profiles available on SI Fig. S4. CR, complete regression.
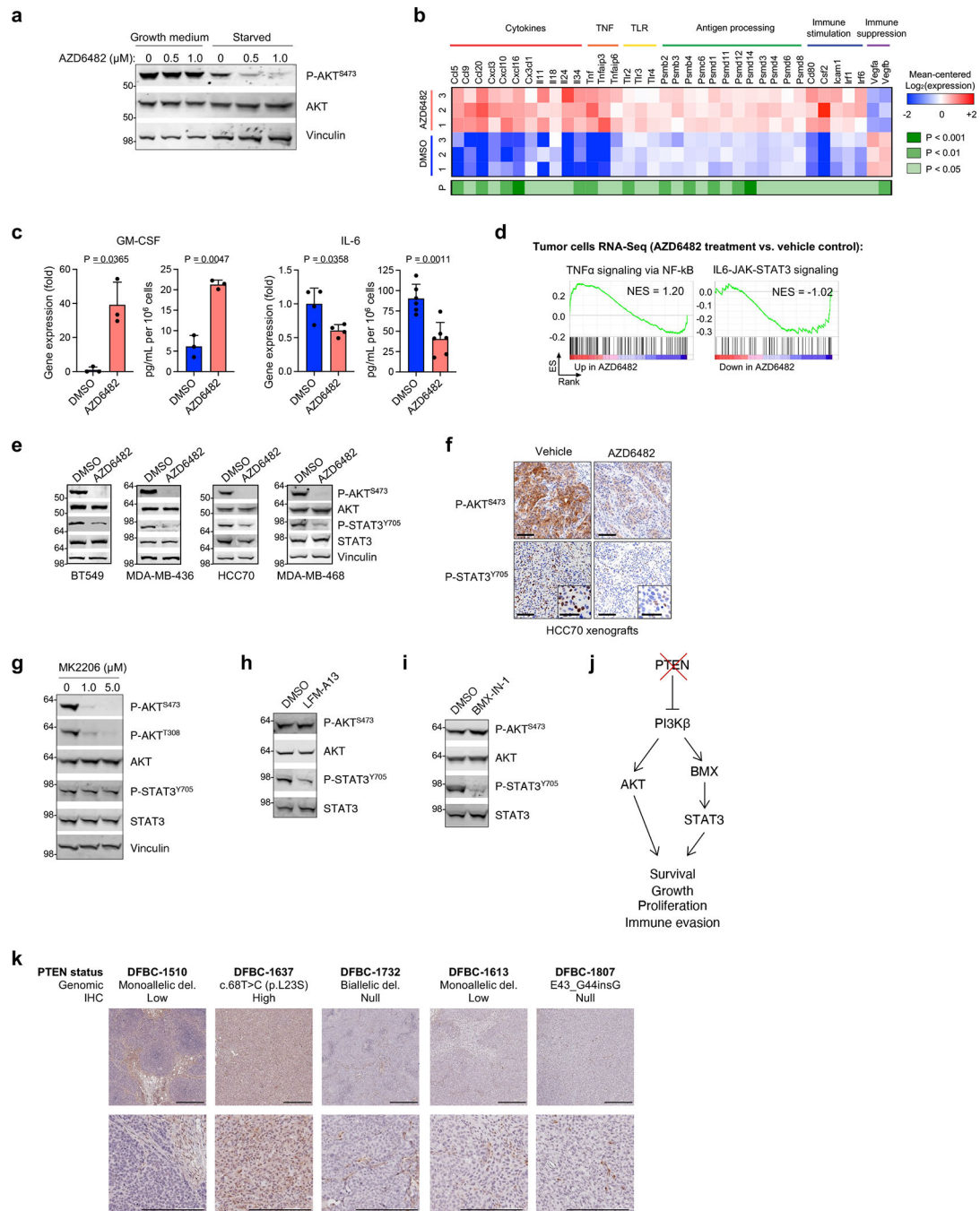
Extended Data Figure 8 |. PI3Kβ regulates STAT3 signaling via TEC Family Kinase BMX.
a, Western blot analysis of PP cells treated with AZD6482 or DMSO as a control
in complete growth media or under serum/nutrient starvation conditions. Immunoblot
representative of two independent experiments. **b-c**, Analysis of PP cells treated with
AZD6482 under serum/nutrient starvation by gene expression (**b**; n = 3 biological replicates
per condition), and Q-PCR (GM-CSF, n = 3 biological replicates per group; IL-6, n =
4 biological replicates per group) and ELISA (GM-CSF, n = 4 biological replicates per
group; IL-6, n = 6 biological replicates per group) (**c**). For comparison of two means,

unpaired, two-tail t-test with Welch's correction assuming unequal variance. Data in (**c**) presented as mean values and s.d. **d**, PP tumor-bearing nude mice were treated with a vehicle control or AZD6482. RNA from isolated tumor cells was analyzed by RNA-Seq. Results from GSEA for AZD6482 compared to vehicle are shown (n = 3 tumors per group). **e**, Western blot analysis of PTEN-deficient human breast cancer cells treated with AZD6482 or DMSO as a control under reduced nutrient/serum conditions. Immunoblots representative of two biological replicates per condition. **f**, Immunohistochemistry analysis of HCC70 xenografts from nude mice treated with AZD6482 or a vehicle control. Representative images shown (n = 5 tumors per condition). Scale bars = 100 μm and 50 μm (inset). **g-i**, Western blot analysis of PP cells treated with the AKT inhibitor MK2206 (**g**), the TEC Kinase family inhibitor LFM-A13 (**h**) or the BMX inhibitor BMX-IN-1 (**i**) under serum/ nutrient starvation conditions. Immunoblots representative of two independent experiments performed in duplicate. **j**, Molecular mechanisms working model. **k**, Summary of PDX models denoting *PTEN* genomic status and PTEN protein levels as assessed by IHC. Representative IHC sections are shown (n = 2 tumors per model). Scale bars, 300 μm. Apparent molecular weights in kDa are indicated for immunoblots.
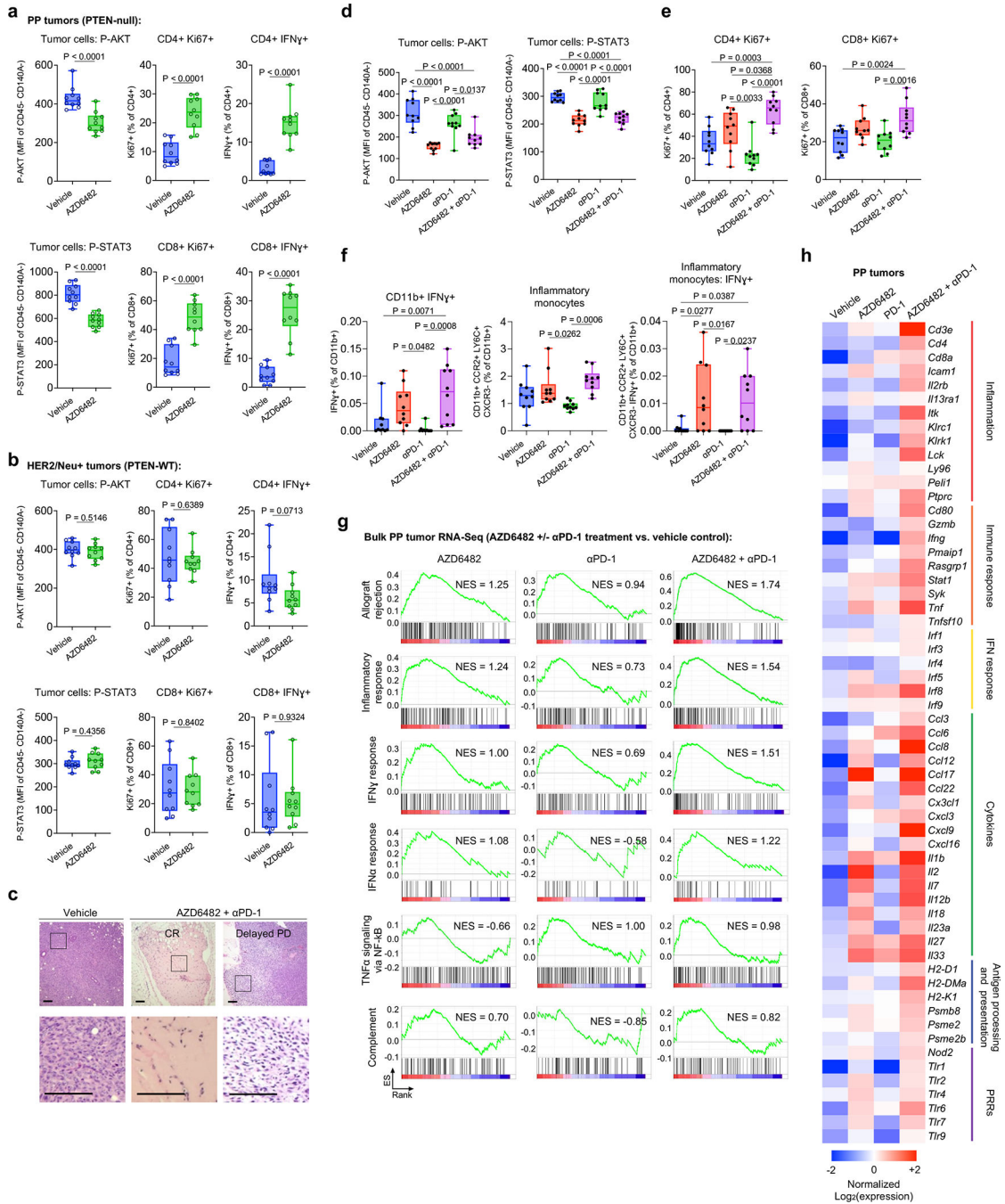
Extended Data Figure 9 |. PD-1 blockade potentiates anti-tumor immune response induced by PI3Kβ inhibition in PTEN-null mouse mammary tumors.

a-b, Flow cytometry analysis of tumor cells and immune infiltrate from PP (**a**) or HER2/Neu+ (**b**) tumors harvested from FVB mice treated with AZD6482 or a vehicle control (n = 10 tumors per condition). **c**, H&E stain of representative tumor samples from mice (Exp. 1) treated with vehicle (n = 8) or combined AZD6482 and PD-1 blockade (αPD-1), including cases showing complete response (CR; n = 3) and delayed progressive disease (PD; n = 3). Scale bars = 100 μm. **d-f**, Flow cytometry analysis of tumor cells and immune infiltrate

from PP tumor-bearing FVB mice treated with AZD6482 or αPD-1 as single agents or in combination (n = 10 tumors per group). Box plots represent median and inter-quartile range, and min-to-max error bars (whiskers). For comparison of two means (**a-b**), unpaired, two-tail t-test with Welch's correction assuming unequal variance. For multiple comparisons (**d-f**), one-way ANOVA followed by Tukey's multiple comparisons tests. **g-h**, RNA from bulk PP tumor fragments was analyzed by RNA-Seq (n = 6 per group). Results from GSEA compared to the vehicle control (**g**) and heatmap denoting expression of immune-related genes (**h**) are shown. Flow cytometry gating profiles available on SI Fig. S5–S6. MFI, mean fluorescence intensity; IFN, interferon; NES, normalized enrichment score; PRRs, pattern recognition receptors.
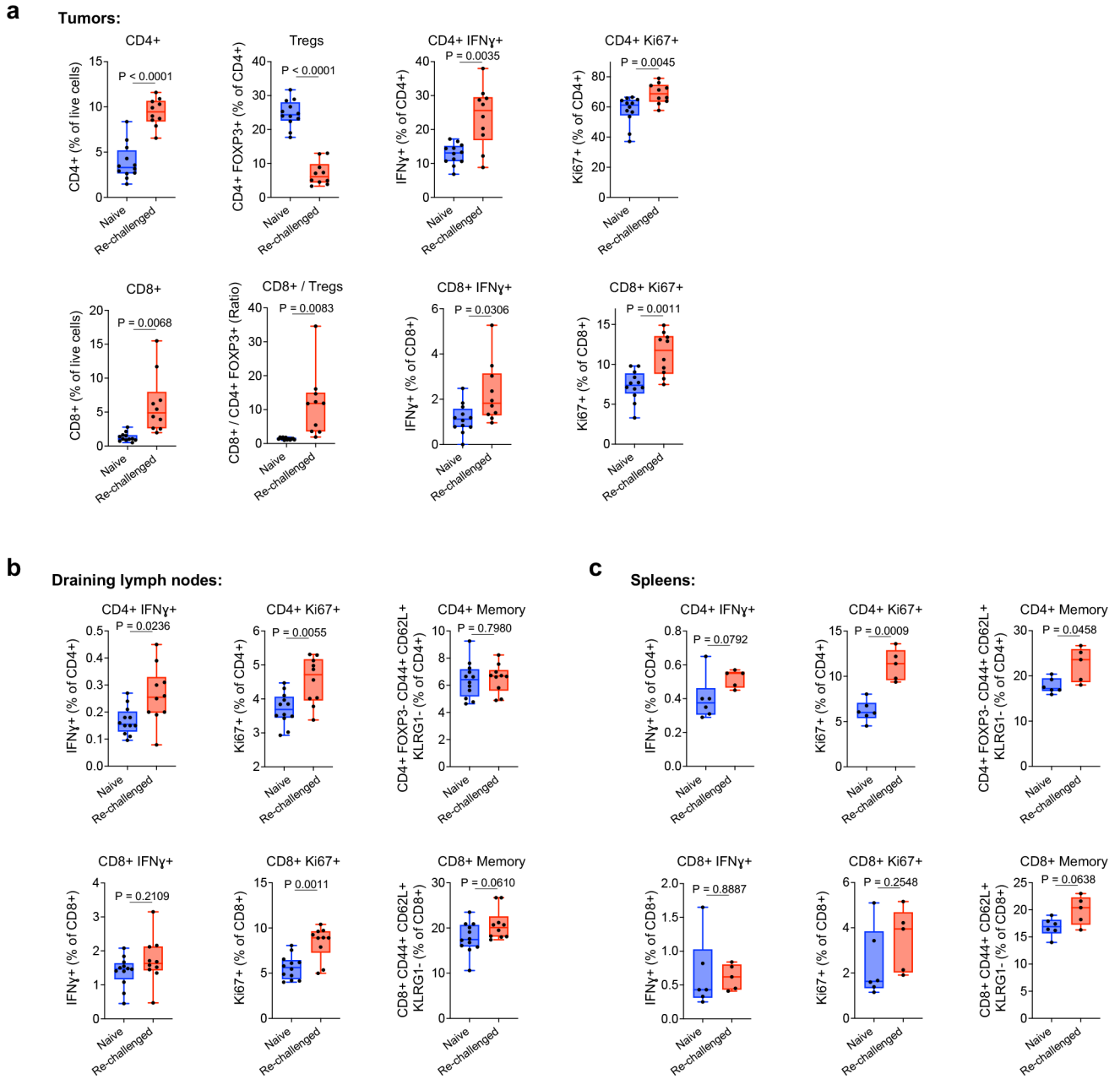
Extended Data Figure 10 |. Mice with complete response to combined PI3Kβ inhibition and PD-1 blockade exhibit robust anti-tumor immunity to tumor re-challenge.

a-c, Flow cytometry analysis of tumor immune infiltrate (**a**; n = 12 tumors for naïve; n = 10 tumors for re-challenged), draining lymph nodes (**b**; n = 12 lymph nodes for naïve; n = 10 lymph nodes for re-challenged) and spleens (**c**; n = 6 spleens for naïve; n = 5 spleens for re-challenged) from age-matched FVB mice challenged for the first time (naïve; n = 6 mice) and in mice with complete response to combined treatment and challenged for a second time (re-challenged; n = 5 mice). Tissues were harvested two weeks after re-challenging. Box plots represent median and inter-quartile range, and min-to-max error bars (whiskers). For comparison of two means, unpaired, two-tail t-test with Welch's correction assuming

unequal variance. Flow cytometry gating profiles available on SI Fig. S7. MFI, mean fluorescence intensity; Tregs, regulatory T-cells.
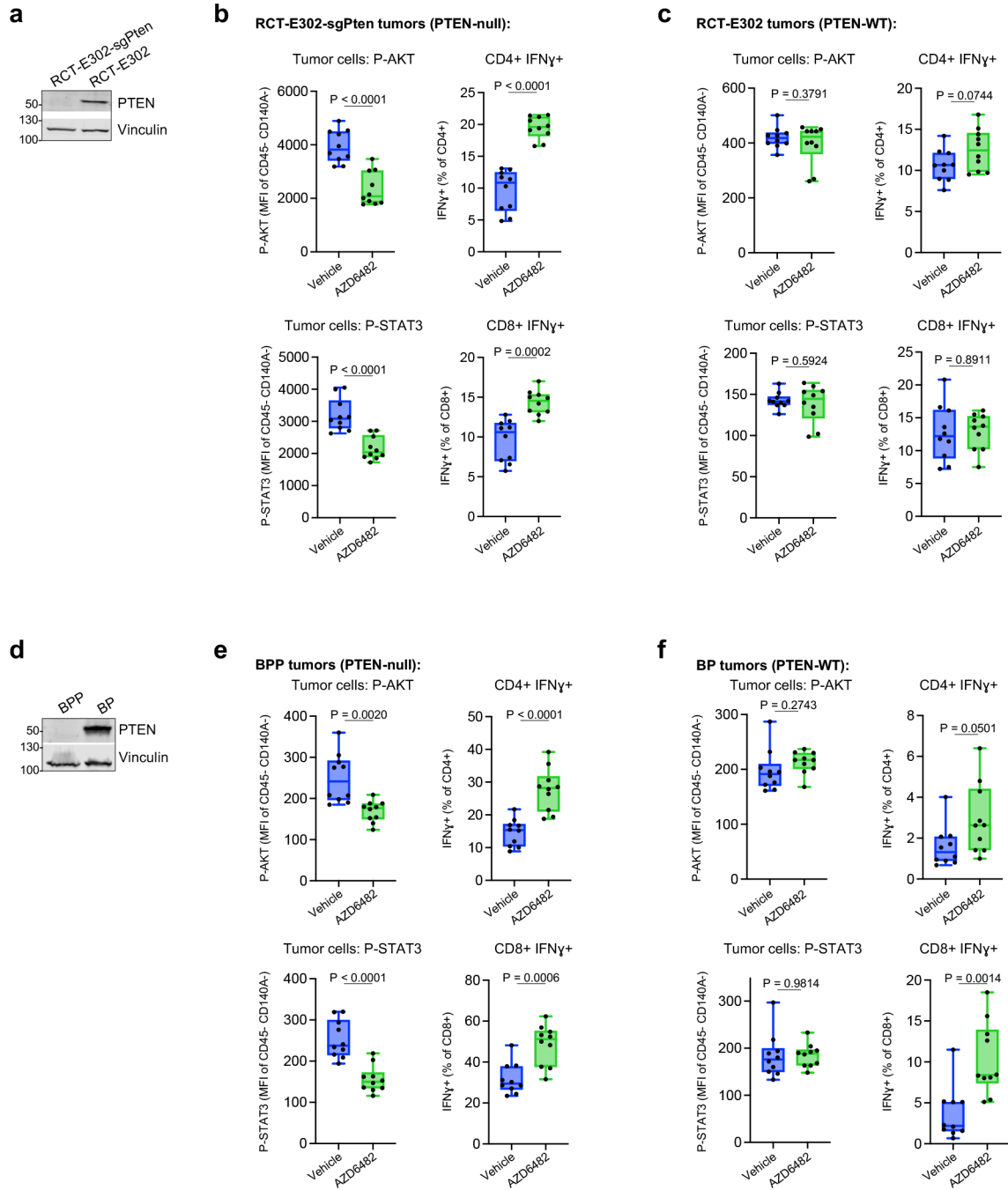
Extended Data Figure 11 |. PTEN loss sensitizes tumors to enhancement of anti-tumor immune response by pharmacological PI3Kβ-specific inhibition.
a, Western blot analysis of RCT-E302 mouse mammary tumor cells with deleted *Pten* (RCT-E302-sgPten) and parental RCT-E302 cells. **b-c**, Flow cytometry analysis of tumor cells and immune infiltrate from RCT-E302-sgPten (**b**) or RCT-E302 (**c**) tumors harvested from FVB mice treated with AZD6482 or a vehicle control (n = 10 tumors per group). **d**, Western blot

analysis of BPP (*Brca1/Trp53/Pten* triple-null) and BP (*Brca1/Trp53* double-null) mouse mammary tumor cells. **e-f**, Flow cytometry analysis of tumor cells and immune infiltrate from BPP (**e**) or BP (**f**) tumors harvested from FVB mice treated with AZD6482 or a vehicle control (n = 10 tumors per group). Apparent molecular weights in kDa are indicated for immunoblots. For comparison of two means (**b-c** and **e-f**), unpaired, two-tail t-test with Welch's correction assuming unequal variance. Flow cytometry gating profiles available on SI Fig. S8.
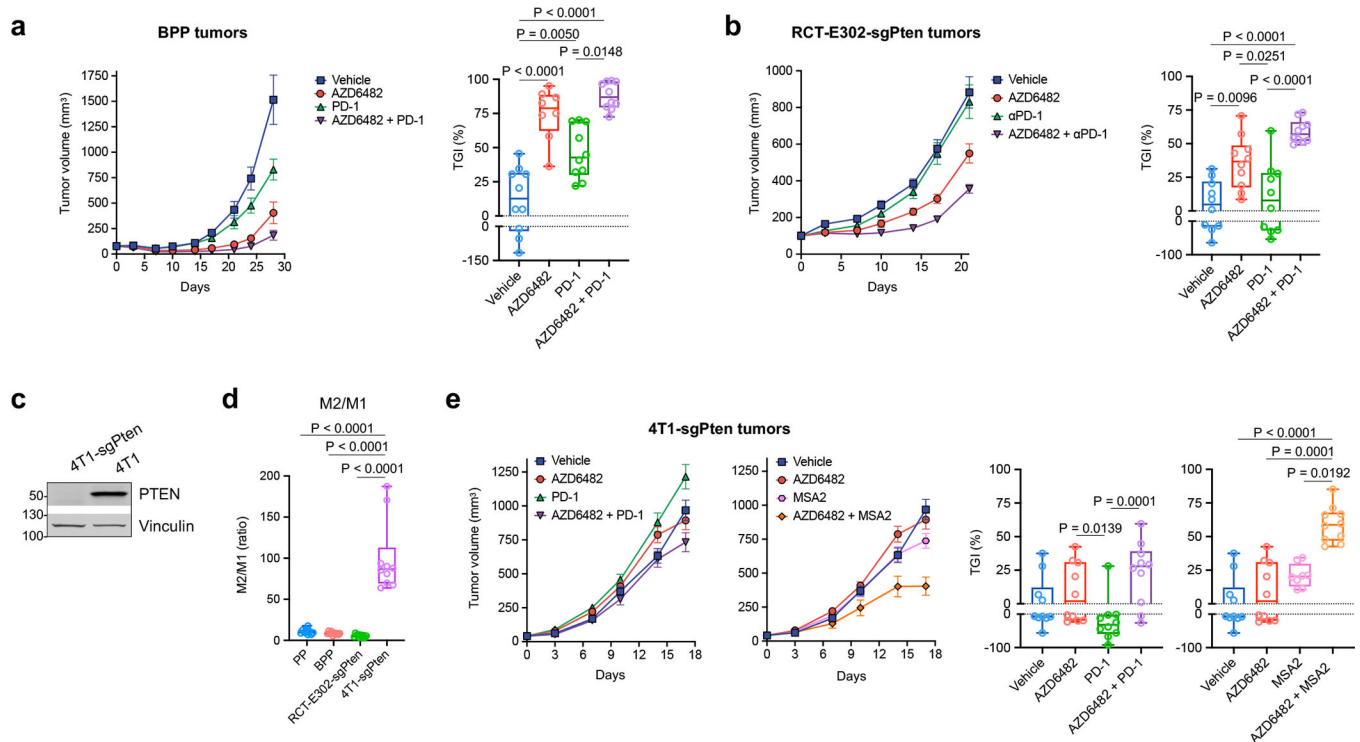
Extended Data Figure 12 |. Combined PI3Kβ inhibition and immunotherapy inhibit tumor growth in mouse models of PTEN-null breast cancer.

a-b, Tumor-bearing mice were treated with AZD6482 or a monoclonal antibody against mouse PD-1 (αPD-1) alone or in combination, as shown. Tumor growth curves (left panels) and tumor growth inhibition (TGI; right panels) are shown (n = 8 tumors for AZD6482 in (**a**); n = 10 tumors for other conditions in (**a**) and (**b**)). **c**, Western blot analysis of 4T1 mouse mammary tumor cells with deleted *Pten* (4T1-sgPten) and parental 4T1 cells. Image is representative of two independent immunoblots. Apparent molecular weights in kDa are indicated. **d**, Ratio of M2-like polarized (CD206^{High} MHC-II-) to M1-like polarized (CD206- MHC-II^{High}) macrophages (CD11b+ F4/80+) as determined by flow cytometry (n = 10 tumors per group). **e**, 4T1-sgPten tumor-bearing mice were treated with AZD6482, αPD-1 or the STING agonist MSA2 alone or in combination. Tumor growth curves (left panels) and TGI (right panels) are each shown as two separate plots for clarity, with all plots including the same vehicle and AZD6482 groups for easier comparison (n = 8 tumors for MSA; n = 10 tumors for other conditions). Data for tumor growth curves presented as mean values and s.e.m. Box plots represent median and inter-quartile range, and min-to-max error bars (whiskers). For comparison of multiple mean values (**a-b** and **d-e**), one-way ANOVA

Author Manuscript

followed by Tukey's multiple comparisons tests. Statistical analysis on (**e**) was performed including all groups in the comparisons, with results shown in two different graphs for easier visual assessment. Flow cytometry gating profiles are available on Supplementary Information Fig. S9.

Supplementary Material

Refer to Web version on PubMed Central for supplementary material.

Data availability

Transcriptomic data for bulk RNA-Seq and single-cell RNA-Seq have been deposited at the Gene Expression Omnibus (GEO) under accession numbers GSE225064 and GSE224906. The scRNA-Seq data has also been uploaded to the Single Cell Portal under accession number SCP2118. Source data are provided for this article.

References

1. Lawrence MS et al. Discovery and saturation analysis of cancer genes across 21 tumour types. Nature 505, 495–501, doi:10.1038/nature12912 (2014). [PubMed: 24390350]

2. Dong Y et al. PTEN functions as a melanoma tumor suppressor by promoting host immune response. Oncogene 33, 4632–4642, doi:10.1038/onc.2013.409 (2014). [PubMed: 24141770]

3. Li S et al. The tumor suppressor PTEN has a critical role in antiviral innate immunity. Nature immunology 17, 241–249, doi:10.1038/ni.3311 (2016). [PubMed: 26692175]

4. George S et al. Loss of PTEN Is Associated with Resistance to Anti-PD-1 Checkpoint Blockade Therapy in Metastatic Uterine Leiomyosarcoma. Immunity 46, 197–204, doi:10.1016/j.immuni.2017.02.001 (2017). [PubMed: 28228279]

5. Parsa AT et al. Loss of tumor suppressor PTEN function increases B7-H1 expression and immunoresistance in glioma. Nature medicine 13, 84–88, doi:10.1038/nm1517 (2007).

6. Peng W et al. Loss of PTEN Promotes Resistance to T Cell-Mediated Immunotherapy. Cancer discovery 6, 202–216, doi:10.1158/2159-8290.CD-15-0283 (2016). [PubMed: 26645196]

7. Jia S et al. Essential roles of PI(3)K-p110beta in cell growth, metabolism and tumorigenesis. Nature 454, 776–779, doi:10.1038/nature07091 (2008). [PubMed: 18594509]

8. Ni J et al. Functional characterization of an isoform-selective inhibitor of PI3K-p110β as a potential anticancer agent. Cancer discovery 2, 425–433, doi:10.1158/2159-8290.CD-12-0003 (2012). [PubMed: 22588880]

9. Wee S et al. PTEN-deficient cancers depend on PIK3CB. Proceedings of the National Academy of Sciences of the United States of America 105, 13057–13062, doi:10.1073/pnas.0802655105 (2008). [PubMed: 18755892]

10. Wang Q et al. Spatially distinct roles of class Ia PI3K isoforms in the development and maintenance of PTEN hamartoma tumor syndrome. Genes & development 27, 1568–1580, doi:10.1101/gad.216069.113 (2013). [PubMed: 23873941]

11. Network CGA Comprehensive molecular portraits of human breast tumours. Nature 490, 61–70, doi:10.1038/nature11412 (2012). [PubMed: 23000897]

12. Szabo PA et al. Single-cell transcriptomics of human T cells reveals tissue and activation signatures in health and disease. Nature communications 10, 4706–4716, doi:10.1038/s41467-019-12464-3 (2019).

13. Zemmour D et al. Single-cell gene expression reveals a landscape of regulatory T cell phenotypes shaped by the TCR. Nature immunology 19, 291–301, doi:10.1038/s41590-018-0051-0 (2018). [PubMed: 29434354]

14. Fu C & Jiang A Dendritic Cells and CD8 T Cell Immunity in Tumor Microenvironment. Frontiers in immunology 9, 3059, doi:10.3389/fimmu.2018.03059 (2018). [PubMed: 30619378]

15. Azizi E et al. Single-Cell Map of Diverse Immune Phenotypes in the Breast Tumor Microenvironment. Cell 174, 1293–1308.e1236, doi:10.1016/j.cell.2018.05.060 (2018). [PubMed: 29961579]

16. Schridde A et al. Tissue-specific differentiation of colonic macrophages requires TGFβ receptor-mediated signaling. Mucosal immunology 10, 1387–1399, doi:10.1038/mi.2016.142 (2017). [PubMed: 28145440]

17. Tuit S et al. Transcriptional Signature Derived from Murine Tumor-Associated Macrophages Correlates with Poor Outcome in Breast Cancer Patients. Cell reports 29, 1221–1235.e1225, doi:10.1016/j.celrep.2019.09.067 (2019). [PubMed: 31665635]

18. Spranger S et al. Up-regulation of PD-L1, IDO, and T(regs) in the melanoma tumor microenvironment is driven by CD8(+) T cells. Science translational medicine 5, 200ra116, doi:10.1126/scitranslmed.3006504 (2013).

19. Iwabuchi R et al. Introduction of Human Flt3-L and GM-CSF into Humanized Mice Enhances the Reconstitution and Maturation of Myeloid Dendritic Cells and the Development of Foxp3+CD4+ T Cells. Frontiers in immunology 9, 1042, doi:10.3389/fimmu.2018.01042 (2018). [PubMed: 29892279]

20. Menezes S et al. The Heterogeneity of Ly6Chi Monocytes Controls Their Differentiation into iNOS+ Macrophages or Monocyte-Derived Dendritic Cells. Immunity 45, 1205–1218, doi:10.1016/j.immuni.2016.12.001 (2016). [PubMed: 28002729]

21. Yu H, Pardoll D & Jove R STATs in cancer inflammation and immunity: a leading role for STAT3. Nature reviews. Cancer 9, 798–809, doi:10.1038/nrc2734 (2009). [PubMed: 19851315]

22. Lien EC, Dibble CC & Toker A PI3K signaling in cancer: beyond AKT. Current opinion in cell biology 45, 62–71, doi:10.1016/j.ceb.2017.02.007 (2017). [PubMed: 28343126]

23. Guryanova Olga A. et al. Nonreceptor Tyrosine Kinase BMX Maintains Self-Renewal and Tumorigenic Potential of Glioblastoma Stem Cells by Activating STAT3. Cancer Cell 19, 498--511, doi:10.1016/j.ccr.2011.03.004 (2011). [PubMed: 21481791]

24. Hart JR, Liao L, Yates JR & Vogt PK Essential role of Stat3 in PI3K-induced oncogenic transformation. Proceedings of the National Academy of Sciences of the United States of America 108, 13247–13252, doi:10.1073/pnas.1110486108 (2011). [PubMed: 21788516]

25. Liu F et al. Discovery of a Selective Irreversible BMX Inhibitor for Prostate Cancer. ACS Chemical Biology 8, 1423--1428, doi:10.1021/cb4000629 (2013). [PubMed: 23594111]

26. Horn LA, Fousek K & Palena C Tumor Plasticity and Resistance to Immunotherapy. Trends in Cancer 6, 432--441, doi:10.1016/j.trecan.2020.02.001 (2020). [PubMed: 32348738]

27. Spranger S, Bao R & Gajewski TF Melanoma-intrinsic β-catenin signalling prevents anti-tumour immunity. Nature 523, 231–235, doi:10.1038/nature14404 (2015). [PubMed: 25970248]

28. Tauriello DVF et al. TGFβ drives immune evasion in genetically reconstituted colon cancer metastasis. Nature 554, 538--543, doi:10.1038/nature25492 (2018). [PubMed: 29443964]

29. Sopasakis VR et al. Specific Roles of the p110α Isoform of Phosphatidylinsositol 3-Kinase in Hepatic Insulin Signaling and Metabolic Regulation. Cell Metabolism 11, 220--230, doi:10.1016/j.cmet.2010.02.002 (2010). [PubMed: 20197055]

30. Schmit F et al. PI3K isoform dependence of PTEN-deficient tumors can be altered by the genetic context. Proceedings of the National Academy of Sciences of the United States of America 111, 6395–6400, doi:10.1073/pnas.1323004111 (2014). [PubMed: 24737887]

31. Wang Q et al. PI3K-p110α mediates resistance to HER2-targeted therapy in HER2+, PTEN-deficient breast cancers. Oncogene 35, 3607–3612, doi:10.1038/onc.2015.406 (2016). [PubMed: 26500061]

32. Liu P et al. Oncogenic PIK3CA-driven mammary tumors frequently recur via PI3K pathway-dependent and PI3K pathway-independent mechanisms. Nature medicine 17, 1116–1120, doi:10.1038/nm.2402 (2011).

33. Wang Q et al. STING agonism reprograms tumor-associated macrophages and overcomes resistance to PARP inhibition in BRCA1-deficient models of breast cancer. Nature Communications 13, 3022, doi:10.1038/s41467-022-30568-1 (2022).

34. Minami A, Nakanishi A, Ogura Y, Kitagishi Y & Matsuda S Connection between Tumor Suppressor BRCA1 and PTEN in Damaged DNA Repair. Frontiers in Oncology 4, 318, doi:10.3389/fonc.2014.00318 (2014). [PubMed: 25426449]

35. Halbrook CJ et al. Macrophage-Released Pyrimidines Inhibit Gemcitabine Therapy in Pancreatic Cancer. Cell Metabolism 29, 1390--1399.e1396, doi:10.1016/j.cmet.2019.02.001 (2019). [PubMed: 30827862]

36. Olson OC, Kim H, Quail DF, Foley EA & Joyce JA Tumor-Associated Macrophages Suppress the Cytotoxic Activity of Antimitotic Agents. Cell reports 19, 101–113, doi:10.1016/j.celrep.2017.03.038 (2017). [PubMed: 28380350]

37. Toso A et al. Enhancing chemotherapy efficacy in Pten-deficient prostate tumors by activating the senescence-associated antitumor immunity. Cell reports 9, 75–89, doi:10.1016/j.celrep.2014.08.044 (2014). [PubMed: 25263564]

38. Noh KH et al. Activation of Akt as a mechanism for tumor immune evasion. Molecular therapy : the journal of the American Society of Gene Therapy 17, 439 -- 447, doi:10.1038/mt.2008.255 (2009). [PubMed: 19107122]

39. Lee H et al. A requirement of STAT3 DNA binding precludes Th-1 immunostimulatory gene expression by NF-κB in tumors. Cancer research 71, 3772–3780, doi:10.1158/0008-5472.CAN-10-3304 (2011). [PubMed: 21502401]

40. Kaneda MM et al. PI3Kγ is a molecular switch that controls immune suppression. Nature 539, 437–442, doi:10.1038/nature19834 (2016). [PubMed: 27642729]

41. Kalinsky K et al. Ipatasertib in Patients with Tumors with AKT Mutations: Results from the NCI-MATCH ECOG-ACRIN Trial (EAY131) Sub-protocol Z1K. European Journal of Cancer 174, S8--S9, doi:10.1016/s0959-8049(22)00824-3 (2022).

42. Turner N et al. Capivasertib and fulvestrant for patients with aromatase inhibitor-resistant hormone receptor-positive/human epidermal growth factor receptor 2-negative advanced breast cancer: Results from the phase III CAPItello-291 trial. Presented at SABC 2022. Abstract GS3–04 (2022).

43. Juric D et al. Phosphatidylinositol 3-Kinase α-Selective Inhibition With Alpelisib (BYL719) in PIK3CA-Altered Solid Tumors: Results From the First-in-Human Study. Journal of clinical oncology : official journal of the American Society of Clinical Oncology, JCO2017727107, doi:10.1200/JCO.2017.72.7107 (2018).

44. Juric D et al. Convergent loss of PTEN leads to clinical resistance to a PI(3)Kα inhibitor. Nature 518, 240–244, doi:10.1038/nature13948 (2015). [PubMed: 25409150]

45. Choudhury AD et al. A Phase I Study Investigating AZD8186, a Potent and Selective Inhibitor of PI3Kβ/δ, in Patients with Advanced Solid Tumors. Clinical Cancer Research 28, OF1--OF13, doi:10.1158/1078-0432.ccr-21-3087 (2022).

46. Dumbrava EE et al. Phase I/II study of the selective PI3Kβ inhibitor GSK2636771 in combination with pembrolizumab in patients (pts) with metastatic castration-resistant prostate

cancer (mCRPC) and PTEN loss. Journal of Clinical Oncology 40, 5052--5052, doi:10.1200/jco.2022.40.16_suppl.5052 (2022).

47. Jung M et al. SO-10 An open-label, multi-centre, phase Ib/II study of PI3Kβ selective inhibitor GSK2636771 administered in combination with paclitaxel in patients with advanced gastric cancer having alterations in PI3K/Akt pathway. Annals of Oncology 32, S206, doi:10.1016/j.annonc.2021.05.034 (2021).

48. Mateo J et al. A First-Time-in-Human Study of GSK2636771, a Phosphoinositide 3 Kinase Beta-Selective Inhibitor, in Patients with Advanced Solid Tumors. Clinical cancer research : an official journal of the American Association for Cancer Research 23, 5981 -- 5992, doi:10.1158/1078-0432.ccr-17-0725 (2017). [PubMed: 28645941]

49. Lu X et al. Effective combinatorial immunotherapy for castration-resistant prostate cancer. Nature 543, 728–732, doi:10.1038/nature21676 (2017). [PubMed: 28321130]

Additional references

50. Simond AM, Rao T, Zuo D, Zhao JJ & Muller WJ ErbB2-positive mammary tumors can escape PI3K-p110α loss through downregulation of the Pten tumor suppressor. Oncogene 36, 6059--6066, doi:10.1038/onc.2017.264 (2017). [PubMed: 28783168]

51. Reardon DA et al. Glioblastoma Eradication Following Immune Checkpoint Blockade in an Orthotopic, Immunocompetent Model. Cancer Immunology Research 4, 124--135, doi:10.1158/2326-6066.cir-15-0151 (2016). [PubMed: 26546453]

52. Palechor-Ceron N et al. Radiation induces diffusible feeder cell factor(s) that cooperate with ROCK inhibitor to conditionally reprogram and immortalize epithelial cells. The American journal of pathology 183, 1862–1870, doi:10.1016/j.ajpath.2013.08.009 (2013). [PubMed: 24096078]

53. Takahashi K & Yamanaka S Induction of pluripotent stem cells from mouse embryonic and adult fibroblast cultures by defined factors. Cell 126, 663–676, doi:10.1016/j.cell.2006.07.024 (2006). [PubMed: 16904174]

54. Lin J-R et al. Highly multiplexed immunofluorescence imaging of human tissues and tumors using t-CyCIF and conventional optical microscopes. eLife 7, doi:10.7554/eLife.31657 (2018).

55. Gierahn TM et al. Seq-Well: portable, low-cost RNA sequencing of single cells at high throughput. Nature methods 14, 395–398, doi:10.1038/nmeth.4179 (2017). [PubMed: 28192419]

56. Hughes TK et al. Highly Efficient, Massively-Parallel Single-Cell RNA-Seq Reveals Cellular States and Molecular Features of Human Skin Pathology. bioRxiv, 689273, doi:10.1101/689273 (2019).

57. Macosko EZ et al. Highly Parallel Genome-wide Expression Profiling of Individual Cells Using Nanoliter Droplets. Cell 161, 1202–1214, doi:10.1016/j.cell.2015.05.002 (2015). [PubMed: 26000488]

58. Butler A, Hoffman P, Smibert P, Papalexi E & Satija R Integrating single-cell transcriptomic data across different conditions, technologies, and species. Nature biotechnology 36, 411–420, doi:10.1038/nbt.4096 (2018).

59. Goel S et al. CDK4/6 inhibition triggers anti-tumour immunity. Nature 548, 471–475, doi:10.1038/nature23465 (2017). [PubMed: 28813415]

60. Krämer A, Green J, Pollard J & Tugendreich S Causal analysis approaches in Ingenuity Pathway Analysis. Bioinformatics 30, 523--530, doi:10.1093/bioinformatics/btt703 (2014). [PubMed: 24336805]

61. Subramanian A et al. Gene set enrichment analysis: A knowledge-based approach for interpreting genome-wide expression profiles. Proceedings of the National Academy of Sciences 102, 15545--15550, doi:10.1073/pnas.0506580102 (2005).

62. Cerami E et al. The cBio cancer genomics portal: an open platform for exploring multidimensional cancer genomics data. Cancer discovery 2, 401–404, doi:10.1158/2159-8290.CD-12-0095 (2012). [PubMed: 22588877]

63. Gao J et al. Integrative analysis of complex cancer genomics and clinical profiles using the cBioPortal. Science signaling 6, pl1–pl1, doi:10.1126/scisignal.2004088 (2013). [PubMed: 23550210]
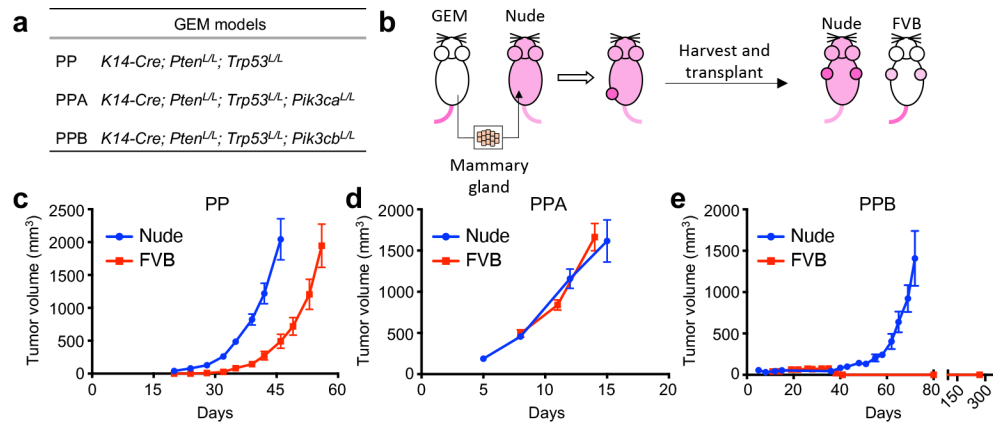
Figure 1 |. PI3Kβ is required for immune evasion in PTEN/p53-deficient invasive breast cancer. **a**, Summary of genetically engineered mouse (GEM) models used in this study. **b**, Strategy for generating *K14-Cre*; *Pten*$^{L/L}$; *Trp53*$^{L/L}$ (PP), *K14-Cre*; *Pten*$^{L/L}$; *Trp53*$^{L/L}$; *Pik3ca*$^{L/L}$ (PPA) and *K14-Cre*; *Pten*$^{L/L}$; *Trp53*$^{L/L}$; *Pik3cb*$^{L/L}$ (PPB) mammary tumors from GEMs. **c-e**, PP, PPA and PPB tumor volume after transplanting into immunodeficient mice (nude; PP, n = 8 tumors; PPA and PPB, n = 4 tumors) or syngeneic immunocompetent mice (FVB; n = 8 tumors per group). Data presented as mean values and s.e.m.
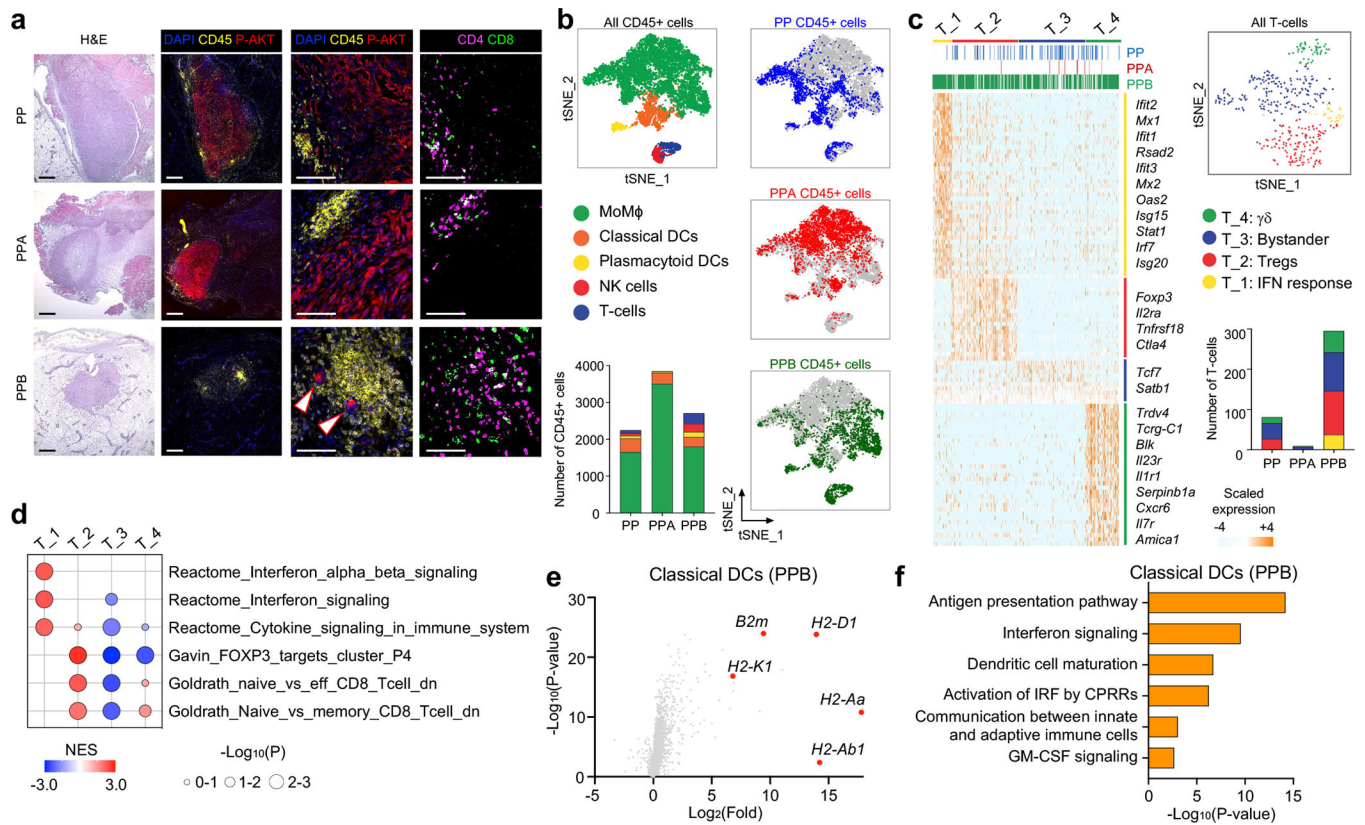
Figure 2 |. PI3Kβ mediates formation of an immunosuppressive microenvironment in PTEN/p53-null breast tumors.

a-i, Analysis of PP, PPA and PPB tumors harvested five days after tumor cell transplantation into FVB mice. **a**, H&E and immunofluorescence analysis of representative sections (n = 3 tumors per group). Tumor cells show positive P-AKT staining (red color). Arrows point to PPB tumor cell clusters. Scale bars, 500 μm (left) and 100 μm (right). **b-f**, Single-cell RNA-Seq analysis of the immune infiltrate (n = 3 mice per group). **b**, Global representation of all cells in the analysis, including tSNE plots denoting cell type and genotype of the tumor of origin, and cell type representation per genotype (stacked columns). **c**, Analysis of T-cell cluster, including heatmap showing gene expression for top 10% differentially-expressed genes (DEGs) for each sub-cluster with selected genes indicated on the right, tSNE of all T-cells analyzed denoting sub-cluster, and sub-cluster representation (absolute numbers of T-cells in analysis) per genotype (stacked columns). Complete list of DEGs per T-cell sub-cluster is available in the source data linked to this article. **d**, GSEA of T-cell sub-clusters. Statistical significance of enrichment scores (p-values) was calculated by GSEA using a phenotype-based permutation test. **e-f**, Analysis of classical dendritic cells (cDCs) from PPB tumors. **e**, Differential gene expression analysis. Statistical significance was calculated using a two-sided Wald test and adjusted for multiple testing using the Benjamini-Hochberg procedure. **f**, Ingenuity pathway analysis of DEGs. Statistical significance was calculated by a right-tailed Fisher's Exact Test.
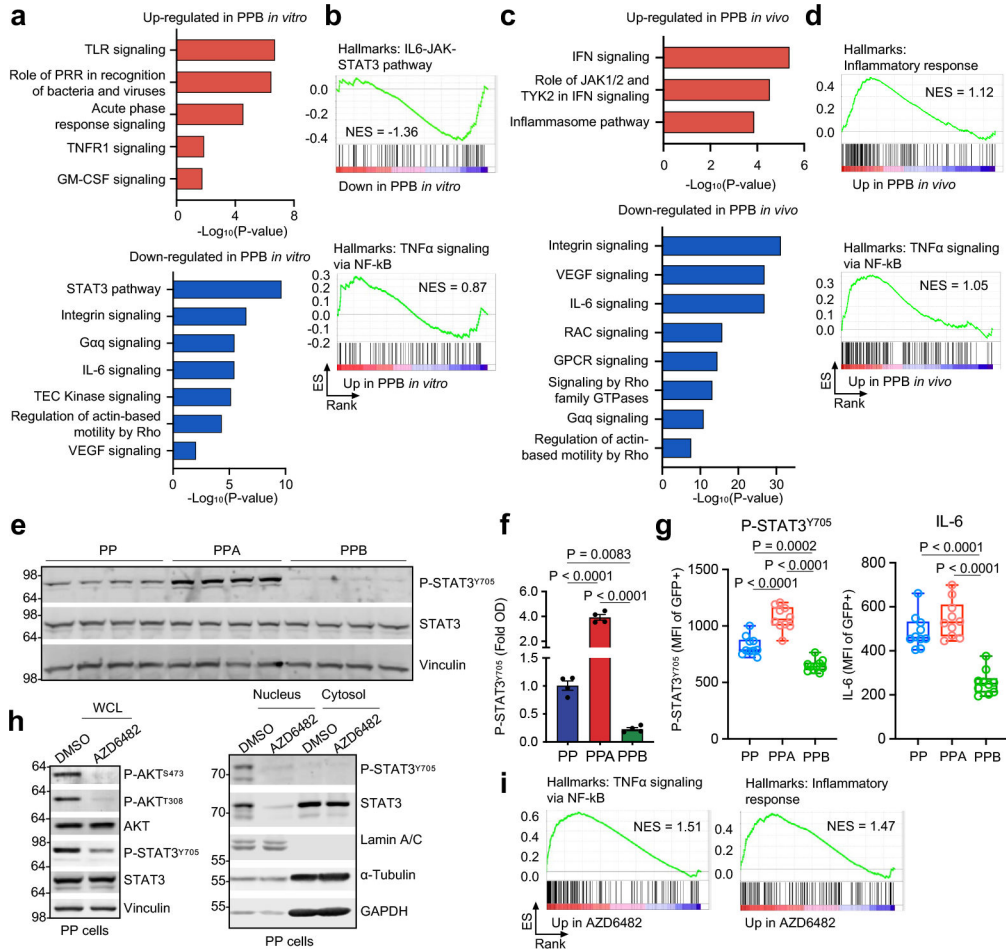
Figure 3 |. PI3Kβ mediates pro-tumor immune signaling in PTEN-deficient breast tumor cells in a STAT3-dependent manner.

a, IPA of differentially-expressed genes (DEGs) in PPB compared to PP cells (n = 3 biological replicates per group) *in vitro*. **b**, GSEA of PPB compared to PP cells (n = 3 biological replicates per group) *in vitro*. **c-d**, Transcriptomic analysis of PP and PPB tumor cells obtained from tumors *in vivo* (n = 4 tumors per group). **c**, IPA of DEGs in PPB compared to PP tumor cells. **d**, GSEA of PPB tumor cells compared to PP. **e-f**, Western blot analysis of primary PP, PPA and PPB cells, including immunoblot image (**e**) and densitometry analysis of P-STAT3^{Y705} levels (**f**; n = 4 biological replicates per group with all samples run on the same immunoblot). Data on (**f**) presented as mean values and s.d. **g**, Flow cytometry analysis of GFP-tagged PP, PPA and PPB tumors harvested from FVB mice five days after inoculation. GFP was added via lentiviral transduction *in vitro* prior to transplantations. Box plots represent median and inter-quartile range, and min-to-max error bars (whiskers). **h-i**, Analysis of PP cells treated with AZD6482 *in vitro* under serum/nutrient starvation by western blotting (**h**) and GSEA (**i**; n = 3 biological replicates per group). Immunoblots representative of three (left) and two (right) independent experiments. Apparent molecular weights in kDa are indicated for immunoblots. Statistical significance for IPA on (**a**) and (**c**) was calculated by a right-tailed Fisher's Exact Test. For comparison of multiple mean values (**f-g**), one-way ANOVA followed by Tukey's multiple comparisons

tests. Flow cytometry gating profiles available on SI Fig. S3. MFI, mean fluorescence intensity; NES, normalized enrichment score; WCL, whole-cell lysate.
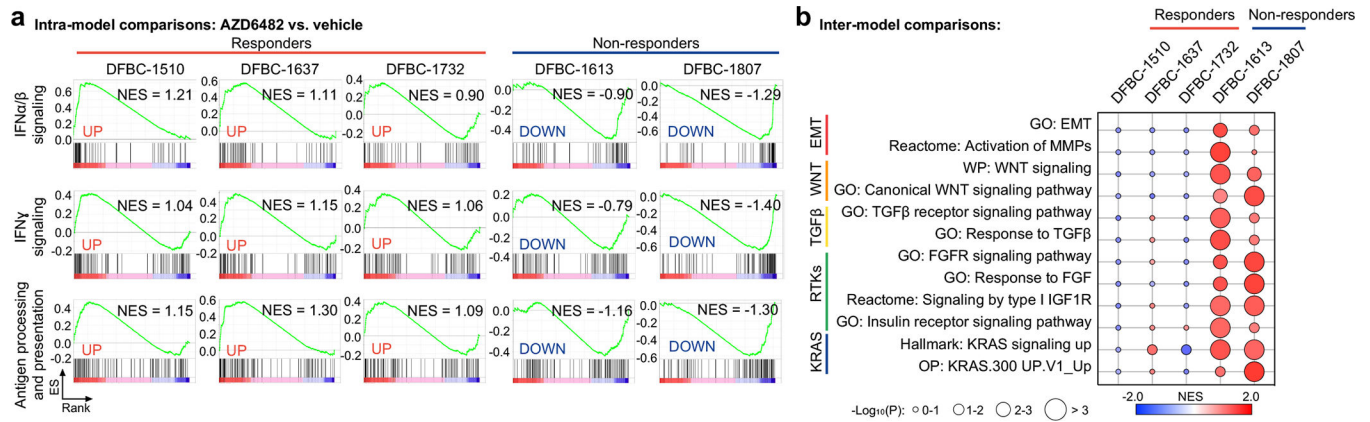
Figure 4 |. Identification of biomarkers of resistance to PI3Kβ inhibition-induced immunity in PTEN-deficient patient-derived xenografts (PDXs).

Mice bearing PTEN-deficient PDXs were treated with AZD6482 for four days. Tumors were harvested and snap-frozen for RNA-Seq analysis (n = 4 tumors per condition for each model). **a**, GSEA comparing AZD6482 treatment to the vehicle control for each individual model. Plots show up- or down-regulation for the AZD6482-treated condition. **b**, GSEA between PDX models (vehicles only). Statistical significance of enrichment scores (p-values) was calculated by GSEA using a phenotype-based permutation test. EMT, epithelial-to-mesenchymal transition; FGF, fibroblast growth factor; FGFR, FGF receptor; GO, gene ontology; IGF1R, insulin-like growth factor 1 receptor; MMPs, matrix metalloproteinases; NES, normalized enrichment score; OP, oncogenic pathways; RTKs, receptor tyrosine kinases; TGFβ, transforming growth factor β; WP, wikipathways
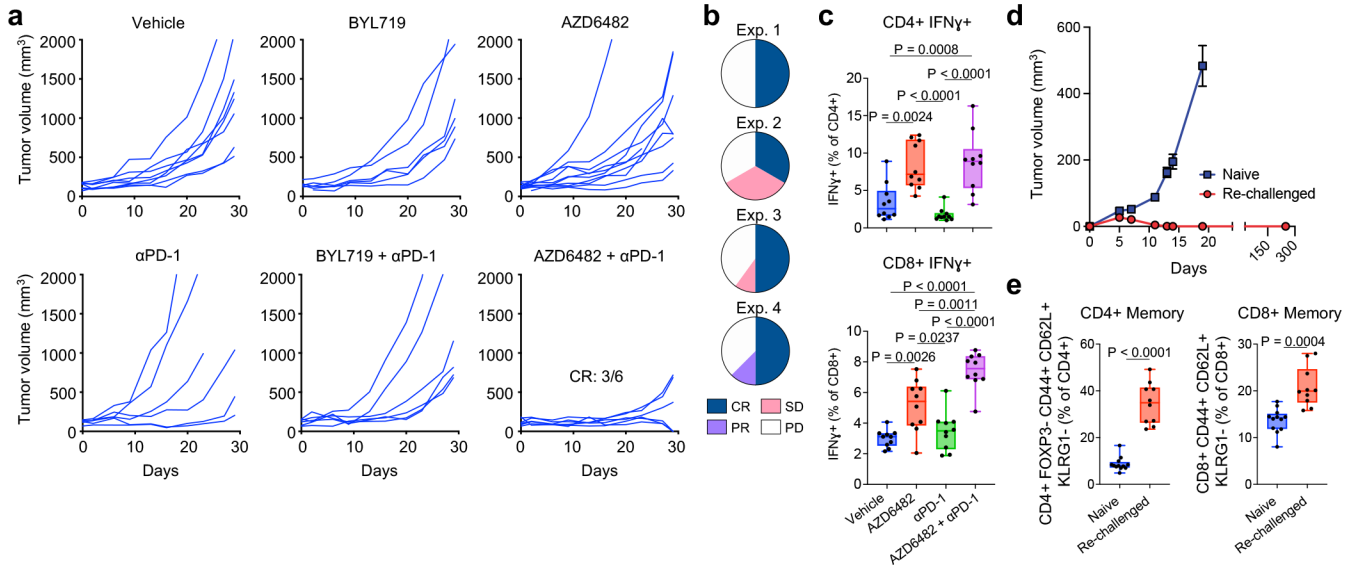
Figure 5 |. Combined PI3Kβ inhibition and PD-1 blockade synergize to inhibit PTEN/p53-null breast tumor growth.

a, PP tumor volume in FVB mice treated with BYL719, AZD6482 or a monoclonal antibody against mouse PD-1 (αPD-1) alone or in combination (Exp. 1). Data shown as growth curve for each individual tumor. Vehicle, n = 8; BYL719, n = 6; AZD6482, n = 10; αPD-1, n = 6; BYL719 + αPD-1, n = 6; AZD6482 + αPD-1, n = 6. **b**, Summary of response for multiple cohorts of mice treated with combined AZD6482 and αPD-1 (Exp. 1–4). Exp. 1, n = 6; Exp. 2, n = 6; Exp. 3, n = 10; Exp. 4, n = 8. **c**, Flow cytometry analysis of PP tumors treated with AZD6482 or αPD-1 as single agents or in combination for 4 days (n = 10 tumors per group). **d**, PP tumor growth in mice challenged for the first time (naïve; n = 10 tumors) and in mice with CR to combined treatment (re-challenged; n = 8 tumors). Data presented as mean values and s.e.m. **e**, Flow cytometry analysis of tumor immune infiltrate from an independent cohort of naïve and re-challenged mice. Tissues were harvested two weeks after re-challenging (naïve, n = 12 tumors; re-challenged, n = 10). Box plots represent median and inter-quartile range, and min-to-max error bars (whiskers). For comparison of two means (**e**), unpaired, two-tail t-test with Welch's correction assuming unequal variance. For multiple comparisons (**c**), one-way ANOVA followed by Tukey's multiple comparisons tests. Flow cytometry gating profiles available on SI Fig. S6–7. CR, complete response; PD, progressive disease; PR, partial response; SD, stable disease.